

The MAGPI Survey: co-evolution of baryons and dark matter in star-forming disk-like galaxies at $0.1 \lesssim z \lesssim 0.85$

Gauri Sharma,^{1,2,3,4,5,*} **Andrew J. Battisti,**^{6,7,8} **Emily Wisnioski,**^{7,8} **J. Trevor Mendel,**^{7,8} **Sabine Bellstedt,**⁶ **Claudia Del P. Lagos,**^{6,8} **Caroline Foster,**^{10,8} **Adriano Poci,**⁹ **Katherine E. Harborne,**^{12,18,19} **Ryan Bagge,**^{10,8} **Stefania Barsanti,**^{11,8} **Joss Bland-Hawthorn**¹¹ **Iris Breda,**¹³ **Scott M. Croom**¹¹ **Karl Glazebrook,**^{20,8} **Yifan Mai,**^{15,16,8} **Sarah M. Sweet,**^{14,8} **Sabine Thater,**¹³ **Lucas M. Valenzuela,**¹⁷ **Glenn van de Ven,**¹³ **Sukyoung Yi,**²¹ **Tayyaba Zafar,**¹⁴ **and Bodo Ziegler,**¹³

¹University of Strasbourg, CNRS UMR 7550, Observatoire astronomique de Strasbourg, F-67000 Strasbourg, France

²SISSA– International School for Advanced Studies, Via Bonomea 265, I-34136 Trieste, Italy

³UWC– University of the Western Cape, Department of Physics and Astronomy, Cape Town 7535, South Africa

⁴IFPU– Institute for Fundamental Physics of the Universe, Via Beirut, 2, 34151 Trieste, Italy

⁵INFN-Sezione di Trieste, via Valerio 2, I-34127 Trieste, Italy

⁶International Centre for Radio Astronomy Research, The University of Western Australia, 35 Stirling Highway, Crawley WA 6009, Australia

⁷Research School of Astronomy and Astrophysics, Australian National University, Cotter Road, Weston Creek, ACT, 2611, Australia

⁸ARC Centre of Excellence for All Sky Astrophysics in 3 Dimensions (ASTRO 3D)

⁹Sub-Department of Astrophysics, University of Oxford, Denys Wilkinson Building, Keble Road, Oxford OX1 3RH

¹⁰School of Physics, University of New South Wales, Sydney, NSW 2052, Australia

¹¹Sydney Institute for Astronomy, School of Physics, A28, The University of Sydney, NSW 2006, Australia

¹²Institute for Computational Cosmology, Physics Department, Durham University, South Road, Durham DH1 3LE, UK

¹Corresponding author: gauri.sharma@astro.unistra.fr

¹³Department of Astrophysics, University of Vienna, Türkenschanzstraße 17, 1180 Vienna, Austria

¹⁴School of Mathematics and Physics, University of Queensland, Brisbane, Qld 4072, Australia

¹⁵Australian Astronomical Optics, Macquarie University, Sydney, NSW 2109, Australia

¹⁶Astrophysics and Space Technologies Research Centre, Macquarie University, Sydney, NSW 2109, Australia

¹⁷Universitäts-Sternwarte, Fakultät für Physik, Ludwig-Maximilians-Universität München, Scheinerstr. 1, 81679 München, Germany

¹⁸Centre for Extragalactic Astronomy, Durham University, South Road, Durham DH1 3LE, UK

¹⁹Department of Physics, Durham University, South Road, Durham DH1 3LE, UK

²⁰Centre for Astrophysics and Supercomputing, Swinburne University of Technology, P.O. Box 218, Hawthorn, VIC 3122, Australia

²¹Department of Astronomy and Yonsei University Observatory, Yonsei University, Seoul 03722, Korea

Abstract.

We present a comprehensive analysis of the dark matter (DM) content and its structural dependence in star-forming disk-like galaxies at intermediate redshifts ($0.1 \lesssim z \lesssim 0.85$), utilizing spatially resolved kinematic data from the Middle Ages Galaxy Properties with Integral Field Spectroscopy (MAGPI) survey. Our sample consists of 266 rotation-supported, main-sequence galaxies. We employ 3DBarolo to model the gas kinematics, obtaining moment maps, surface brightness profiles, rotation velocity profiles, and velocity dispersion profiles. The observed rotation velocity profiles are corrected for inclination and gas pressure support to derive intrinsic rotation curves. By modeling these intrinsic rotation curves and decomposing the total dynamical mass profile into the baryonic and the DM components without employing parametric halo models, we estimate the DM fraction (f_{DM}) within both the effective radius (R_e) and the optical radius (R_{opt}). We report the following: (1) Low stellar mass galaxies ($M_{\text{star}} < 10^{9.5} M_{\odot}$) are strongly DM dominated across all radii, with average $\langle f_{\text{DM}} \rangle \sim 0.85$, while high-mass ($M_{\text{star}} > 10^{10.5} M_{\odot}$) systems exhibit relatively low DM fractions in their inner regions ($\langle f_{\text{DM}} \rangle \sim 0.47$) which is equivalent to local massive disk galaxies (e.g., Milky Way and Andromeda). This suggests a mass-dependent structural dichotomy, most-likely governed by a combination of internal galactic processes and environmental influences. (2) A tight inverse correlation between f_{DM} and baryon mass surface density (Σ_{bar}), with intrinsic scatter of ~ 0.11 dex. This is consistent with an inside-out baryon assembly scenario and suggests that the fundamental structural correlations of galaxies were already established by $z \sim 0.85$. (3) No significant evolution in f_{DM} with redshift across the MAGPI window, and when combined with higher-redshift ($0.6 \leq z \leq 1.5$) data from Sharma et al. 2025, we quantitatively show that the reported decline in $f_{\text{DM}}(z)$ is most-likely due to observational biases against low-mass systems at $z > 1$. These results offer empirical evidence for a scenario in which disk-like galaxies evolve through a co-regulated build-up of baryonic and DM components, preserving internal structural regularities (such as the total mass distribution, and rotation-curve shape) throughout cosmic time.

Contents

1	Introduction	1
2	Dataset	4
2.1	Sample selection	5
2.2	Forward modelling of the data-cubes	9
2.3	Final sample	9
2.4	Rotation curve robustness across emission lines	10
3	Method	11
3.1	Mass modelling of rotation curves	11
3.2	DM fraction	14
3.3	Uncertainties & limitations	15
4	Results & discussion	16
4.1	Dark matter dynamics: scaling f_{DM} with V_c	16
4.2	Dark matter dynamics: scaling f_{DM} with Σ_{bar}	18
4.3	Dark matter dynamics: scaling f_{DM} with z	19
4.4	Statistical relevance of various correlations	21
5	Dark matter evolution with cosmic-time	21
6	Conclusions	25
A	Appendix A.0	28
B	Appendix B.0	29
C	Appendix C.0	29

1 Introduction

Under the current standard model of cosmological structure formation, dark matter (DM)—an elusive, non-luminous form of matter—is thought to constitute the majority of matter in the Universe [e.g., 1]. Despite its prevalence, DM remains undetected by direct means; its existence is inferred primarily from the gravitational effects it exerts on the visible matter. In particular, the discovery of flat rotation curves in the outer regions of galaxies provided compelling evidence that the visible mass alone is insufficient to explain the observed galactic dynamics [2, 3]. This discrepancy led to the hypothesis that galaxies are embedded in extended DM halos that far outweigh their luminous components in mass [e.g., 2–5]. Furthermore, cosmological models and simulations within the standard cold DM (Λ CDM) framework support the picture that DM halos act as a gravitational scaffolding for galaxy formation and evolution [6, and references therein]. However, this paradigm faces several persistent small-scale challenges [e.g., 7, 8], including the “too big to fail” [9] and the “diversity of rotation curves” [10] problems. These persistent problems highlight that our understanding of DM and baryon evolution in galaxies is incomplete.

In this context, detailed observations of mass distributions within the galaxies offer crucial insights. The fraction of mass contributed by DM versus baryons varies widely with galaxy type, mass, and size, underscoring the crucial role of DM in galaxy dynamics. In nearby star-forming disk galaxies, DM typically accounts for roughly 40–50% of the dynamical mass within the inner region (inside half-light radius R_e), rising to about 70–90% within $\sim 3R_e$ which encompasses most of the galaxy’s light [11–13]. In contrast, nearby early-type galaxies (ellipticals and lenticulars) often show much lower DM contributions in their central regions, sometimes as little as $\lesssim 20\%$ within R_e [14]. However, in massive early-type galaxies (with $M_{\text{star}} \gtrsim 10^{10} M_{\odot}$) the central DM fraction tends to increase with stellar mass, yet their outskirts still reach similarly high DM dominance by the radii that encompass most of the stellar light [70–90% within $\sim 5R_e$; 15]. These differences suggest that the assembly history and baryonic processes (e.g., star-formation) of galaxies are intimately connected with the distribution of DM relative to stars; hence, play a crucial role in shaping galaxy structure.

The rationale is that the baryons are expected to be more centrally concentrated than DM due to their dissipative nature: baryons can cool and condense, whereas collisionless CDM cannot. This naturally leads to galaxy centres becoming more baryon-dominated compared to their outskirts. However, this effect alone does not explain the observed differences in DM fractions between low-mass and massive galaxies. A plausible explanation lies in the interplay between “downsizing” and the evolution of gas accretion in a Λ CDM universe. In the downsizing scenario, supported by local observations (e.g. [16, 17]), massive galaxies form earlier and more rapidly than their low-mass counterparts. According to tidal torque theory [18] and hydrodynamical simulations [19, 20], gas accreted at early times in a Λ CDM universe has lower specific angular momentum and is more filamentary than gas accreted later (see [21] for a review). Such filamentary flows can penetrate deep into galactic potential wells, forming highly concentrated progenitors of present-day massive galaxies [22–25]. In contrast, low-mass galaxies typically assemble later and undergo more extended star formation histories. Later accreted gas, having gained higher specific angular momentum through tidal torques [18], settles at larger radii, encompassing a greater fraction of the halo’s DM relative to the galaxy’s size. Regardless of the details, the way baryons accreted and assembled in galaxies is likely to be fundamental in understanding how concentrated they end up being relative to DM.

In addition to the effects of assembly and accretion history, a further layer of complexity arises from baryonic feedback processes. Intense star formation, supernovae, and active galactic nucleus (AGN) activity can drive powerful gas outflows, which alter the gravitational potential and redistribute both the baryons and DM. Some simulations show that repeated feedback episodes can transform initially steep DM cusps into lower-density cores, reducing the DM fraction in the centers of galaxies over several gigayears [26–32]. Thus, the final distribution of DM and baryons is shaped by a combination of how baryons are accreted, assembled, and subsequently redistributed. Measuring the radial distribution of DM and its evolution with cosmic time is therefore crucial; it not only constrains the fundamental nature of DM but also provides critical tests of galaxy formation theories and feedback models in cosmological simulations.

In the past decade, advances in integral field unit (IFU) surveys have opened new avenues for studying galaxies’ internal kinematics out to high redshift. IFU observations now enable the construction of spatially resolved observations (e.g., velocity maps and rotation curves) of galaxies up to $z \sim 6$ [e.g., 33–35], allowing direct probes of the distribution of baryonic and dark mass in distant galaxies. Early IFU studies of high- z star-forming galaxies

(SFGs) yielded surprising results. For example, [36] analysed a sample of 7 high-redshift ($z \approx 0.6 - 2.6$) SFGs and [37] extended this to 101 systems using staking method, finding that high-redshift (hereafter high- z) galaxies show declining outer rotation curves. Such a decline is uncommon among typical local star-forming disk galaxies (which generally have flat rotation curves), being observed locally only in a few extremely massive, high surface-brightness disks [e.g., 2, 38]. Genzel et al. and Lang et al. argued that the falling rotation curves (beyond $1.5R_e$) at high- z could be explained by a combination of very high baryon fractions in the galaxy centers and significant pressure support from turbulent gas. Similarly, other high- z studies of both late-type and early-type galaxies have reported relatively low DM fractions within the R_e [e.g., 39–46].

However, results on the DM content in high- z star-forming galaxies have not yet converged. For example, [47] examined the *stacked* (averaged) rotation curves of ~ 1500 SFGs across $0.6 \lesssim z \lesssim 2.2$. They found that stacked rotation curves are flat out to large radii, closely resembling those of local SFGs. Moreover, their analysis indicated substantial DM contributions: more than 50% of the total mass within $3.5R_e$, in-line with typical local disk galaxies [12, 13, 38]. In another study [48] applied 3D forward modelling to data from the KMOS Redshift One Spectroscopic Survey (KROSS; [49], [50]) to derive *individual* rotation and velocity dispersion curves for galaxies at $z \sim 1$. By correcting for beam-smearing and pressure support, they recovered the intrinsic rotation curves of over 200 rotation-supported disks, finding that most of the rotation curves are flat out to $3R_e$. In [51], the authors used the [48] intrinsic rotation curves and employed a halo model independent method to estimate the DM content. They showed that galaxies are DM dominated across the galactic scales.

Extending this analysis, [52, hereafter GS25] applied the same methodology as [48, 51] to a sample of 263 individual rotation-supported SFGs spanning $0.6 \leq z < 2.5$, including the above KMOS samples, the largest high- z sample with resolved kinematics to-date. They found that the majority ($\sim 75\%$) of these galaxies have DM dominated outer disks, with DM contributing between 50 – 90% of the total mass within R_e out to R_{out} .¹ A recent study by [53] independently confirm these findings using a halo-model dependent approach, further solidifying the evidence that high- z disks generally have massive DM halos, also see [54]. Although there is growing evidence that support the flat rotation curves and DM dominated galaxies at high- z , limitations such as a small sample size, heterogeneous dynamical modelling techniques, and lack of resolved kinematics at intermediate redshifts ($0.1 \leq z < 0.6$) have prevented us from drawing a coherent picture of DM and baryon co-evolution over cosmic time.

In this work, we address the aforementioned limitations. We present a comprehensive study of DM fraction at the intermediate-redshift range ($0.1 \lesssim z \lesssim 0.85$), utilizing spatially resolved kinematics from the Middle Ages Galaxy Properties with Integral Field Spectroscopy (MAGPI) survey [55]. It is a Large Program (Program ID: 1104.B-0536) using Multi-Unit Spectroscopic Explorer (MUSE) on the Very Large Telescope (VLT) at European Southern Observatory (ESO), delivering high-resolution spectroscopy of both stars and ionized gas at a median redshift of $\langle z \rangle \sim 0.35$ (corresponding to look-back times of 3 – 4 Gyr). We

¹In general, the scale length (or characteristic radius) are associated with various quantities that decrease exponentially such as the surface brightness. The stellar disk edge is defined as $3.2 R_D$ ($= 1.89 R_e$), where the stellar surface luminosity $\propto \exp(-r/R_D)$. Therefore, disk scale lengths in terms of the effective radius: $R_D = 0.59 R_e$. Based on studies of local disk galaxies [38], the radius enclosing 80% of the stellar light is called optical radius $R_{\text{opt}} = 1.89 R_e$, while the outer radius (R_{out}), corresponding to 99% of the stellar light, is $R_{\text{out}} = 2.95 R_e$ [48].

provide the details of the survey and dataset in Section 2. In particular, we will employ the same methodology as used by [GS25](#), which is briefly outlined in Section 2.2 & 3. We present and discuss the results in Section 4. Finally, we combine the MAGPI dataset with the [GS25](#) sample, a statistically robust sample of 529 star-forming galaxies, enabling quantitative analysis of baryon and DM co-evolution as a function of galaxy mass, spatial scale, and redshift, which is discussed in Section 5. A summary of the main findings is provided in Section 6. Throughout this analysis, we assume a flat Λ CDM cosmology with $\Omega_{m,0} = 0.27$, $\Omega_{\Lambda,0} = 0.73$, and $H_0 = 70 \text{ km s}^{-1} \text{ Mpc}^{-1}$.

2 Dataset

Using the MUSE on the VLT, the MAGPI survey is designed to investigate the spatially resolved stellar and ionized gas properties of galaxies at lookback times of 3–4 Gyr ($\langle z \rangle \approx 0.35$). The survey targets 60 primary galaxies at $z \sim 0.3$ with stellar masses $M_{\text{star}} > 7 \times 10^{10} M_{\odot}$, along with ~ 100 satellite galaxies spanning a range of environments—from isolated systems to galaxies in groups and clusters. Of these, 56 primary targets were selected from the GAMA survey [\[56, 57\]](#), with the remaining four drawn from archival MUSE observations of the Abell 370 [\[58, 59\]](#) and Abell 2744 [\[60, 61\]](#) fields.

Observations were conducted using the MUSE Wide Field Mode, covering a wavelength range of 4650–9300 Å with a spectral sampling of 1.25 Å. Each MAGPI pointing spans a $1' \times 1'$ field of view centered on a primary target. The spatial sampling is 0.2'' per pixel, and the typical point spread function (PSF) full width at half maximum (FWHM) achieved in the *R*-band is $\sim 0.55''$. Each field was observed in six observing blocks, each comprising two exposures of 1320 sec, totaling 4.4 hours per field and 246 hours of on-source time for the full survey. Observations employed a ground-layer adaptive optics (GLAO) system to enhance image quality, resulting in a spectral gap between 5780–6050 Å due to the sodium laser notch filter of the GALACSI system [\[62\]](#).

A detailed description of the data reduction will be provided in Mendel et al. (in preparation). Briefly, reduction is based on the MUSE-pipeline [PY-MUSEPIPE](#) [\[63\]](#), with sky subtraction performed using the Zurich Atmosphere Purge (ZAP) software [\[64\]](#). For each detected source, a ‘minicube’ is extracted from the full MUSE datacube, centered on the galaxy and encompassing the maximum extent of its ‘dilated’ segmentation map, as determined by [PROFOUND](#) [\[65\]](#). All MUSE extensions—PRIMARY, DATA, STAT, LSF, PSF, EXPOSURE—are retained, and two mask extensions are added to encode the dilated and undilated segments (MASK, MASKUNDILATED).² Spectral modelling of the ‘minicubes’ is performed by Battisti et al. (in preparation) using [GIST v3.0](#) [\[66\]](#), with outputs resampled back onto the native MUSE wavelength grid. The resulting data cubes preserve the $[x, y, z]$ structure and include best-fit stellar continuum, emission line models, and residual spectra (minicube – [continuum + emission]).

Morphological parameters such as axis-ratios (b/a) and effective radius (R_e) are derived from 2D surface brightness modelling using [ProFit](#) [\[67\]](#), assuming a single Sérsic component. The fitting is done in the MAGPI *i*-band (i.e. on a mock *i*-band image computed from the respective MAGPI datacube) using the `scipy.optimize.minimize` function and the ‘Nelder-Mead’ method. To obtain the inclination angle (θ_i), we use these axis-ratios and convert it into

²The software [MPDAF](#) is used to produce the minicubes.

inclination according to:

$$\cos^2 \theta_i = \frac{(b/a)^2 - q_0^2}{1 - q_0^2} \quad (2.1)$$

where q_0 is the intrinsic axial ratio of an edge-on galaxy (e.g. [68]), which could in principle have values in the range $0.1 - 0.65$ (e.g. [69]); here, we use the commonly assumed value $q_0 = 0.2$, which is applicable for thick discs commonly found at high- z [70]; this value is also often adopted at low- z [e.g., 71–73]. Spectroscopic redshifts are estimated using Manual and automatic redshifting software, **MARZ** [74].

Star-formation rates: We adopt integrated star-formation rates (SFRs) estimated from 1D Balmer line flux ratio measurements extracted within the dilated segmentation masks (Battisti et al., in preparation). Observed deviations from these intrinsic line ratios can be attributed to dust reddening [75], with shorter wavelengths being more absorbed than longer wavelengths (e.g., H_β appears fainter relative to H_α than the expected ratio). For the intrinsic line ratios, we assume Case-B recombination, with $T_e = 10^4 K$ and $n_e = 100 \text{ cm}^{-3}$ [75]. Dust attenuation is corrected using the Milky Way extinction curve from [76]. The effect of dust reddening is stronger for lines that are more separated in wavelength, and the uncertainties on dust corrections are generally larger when using line ratios that are closer in wavelength (e.g., H_γ/H_δ instead of H_α/H_β). This is factored into the SFR uncertainties. Finally, line ratios fluxes are converted to SFRs following the calibration of [77, $SFR = 5.5 \times 10^{-42} L_{H\alpha}$], which assumes a [78] initial mass function (IMF). When $H\alpha$ is not available ($z > 0.4$), we use dust corrected H_β or other emission lines to estimate SFR by adopting the assumed case-B recombination intrinsic line ratios (e.g., $F_{H_\alpha} = 2.86 F_{H_\beta}$).

Stellar masses: Stellar masses are derived from broad-band photometry (of $ugriZYJHK_s$, bands) by fitting the spectral energy distributions (SEDs) using the **ProSpect** code [67]. The fits utilize stellar population synthesis models from [79]. Dust attenuation of stellar light is modeled following the two-component prescription of [80], and dust emission is implemented using the dust templates of [81]. For full methodological details, we refer the reader to [82].

We compared SFRs for the full sample derived from SED fitting with those estimated from Balmer emission lines and found a systematic offset of approximately 0.07 dex. This offset is propagated when estimating the uncertainties on the dark matter fraction. In general, broadband SED-based SFRs are higher than those derived from Balmer decrement measurements; however, for high-stellar-mass galaxies ($M_{star} \geq 10^{10.5} M_\odot$), the SED-based SFRs can be up to two orders of magnitude lower than the Balmer-derived values. It should be noted that SED-derived SFRs are intrinsically more uncertain, as the fits are based solely on $ugriZYJHK_s$ broadband photometry and lack far-infrared (FIR) coverage, which limits constraints on dust attenuation.

2.1 Sample selection

We utilize data from 53 out of 60 observed MAGPI fields, comprising minicubes for approximately 2600 galaxies spanning the redshift range $z \approx 0.1 - 0.85$. Our primary selection includes galaxies with confirmed spectroscopic redshifts. From this set, we identify galaxies with *resolved* gas emission in one or more of the following lines: $H\alpha$ (6563 Å), [OIII] (4969 Å), and [OIII] (5008 Å). As discussed in Section 2.4 and demonstrated in Figure 4, these different emission lines, despite variations in line strength and ionization potential, consistently trace

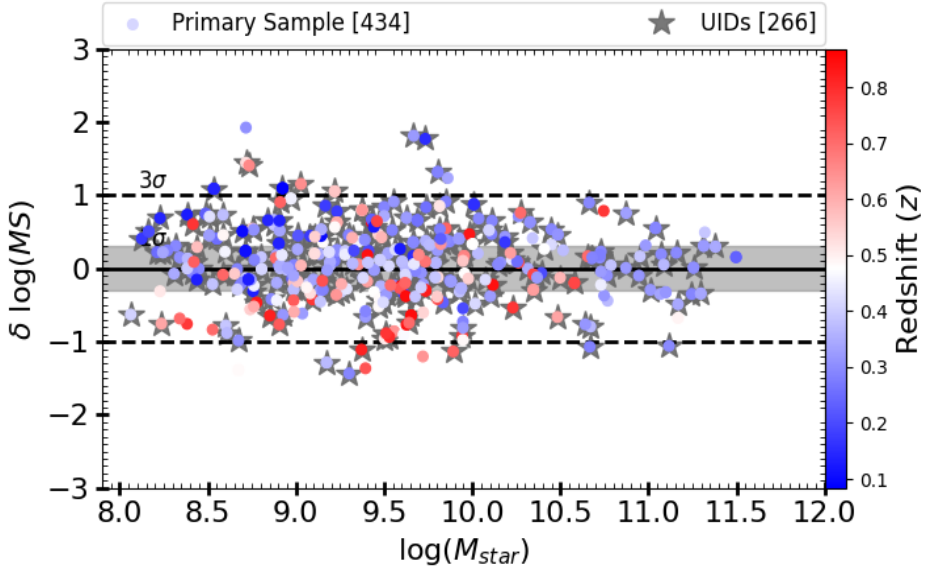


Figure 1. Offset from the star-forming main sequence (MS) as a function of stellar mass (M_{star}). The vertical axis shows the logarithmic deviation from the MS, defined as $\delta \log(\text{MS}) = \log(\text{SFR}/\text{SFR}_{\text{MS}}; (z, M_{\text{star}}))$, where SFR_{MS} is the redshift- and mass-dependent main sequence relation from [83]. Full primary MAGPI sample ($N = 434$) sample is represented by circles color coded for redshift, and the gray stars highlight the number of Unique IDs selected after applying kinematic modelling quality cuts. The gray shaded area represents the 1σ scatter of [83] MS relation. The majority of galaxies lie within the $\pm 2 - 3\sigma$ range of the [83] MS relation, i.e., final sample is consistent with a population of star-forming galaxies.

the same underlying gravitational potential. Therefore, we decided to use multiple emission lines to expand, both, the statistical power of the sample and enhances the reliability of the kinematic and dynamical inferences drawn from the dataset. Hence, a galaxy remains in the work sample if at-least one of these lines are present in the corresponding minicube, and a galaxy is repeated if it has multiple aforementioned emission lines.³ Stellar continuum is subtracted using spectral fits obtained from the GIST pipeline, after which we calculate the integrated signal-to-noise ratio (SNR), within the square aperture each-side covering 30 spaxels ($6.2''$), of the representative emission line around the central wavelength. Galaxies are retained only if their globally integrated emission line exhibits an average $SNR > 3$ within the Gaussian fit. Additionally, we exclude galaxies located at the edge of the minicubes to avoid boundary artifacts.

To mitigate projection effects in the kinematic analysis—such as radial or tangential motions and extinction-induced distortions that leads to a flattened velocity profile—we select only galaxies with intermediate inclinations in the range $25^\circ \leq \theta_i \leq 75^\circ$. We further restrict the sample to galaxies with stellar masses in the range $M_{\text{star}} = 10^8 - 10^{11.5} M_{\odot}$, consistent with the mass distribution of local disk galaxies. This sample is referred to as primary sample, with the majority (99%) of galaxies lying within the $2 - 3\sigma$ range of the star-forming main sequence (SFMS) defined by [83], as shown in Figure 1. We note that the final sample is

³Final measurement of dark matter fraction of repeated galaxies are weighted as discussed in Section 2.4.

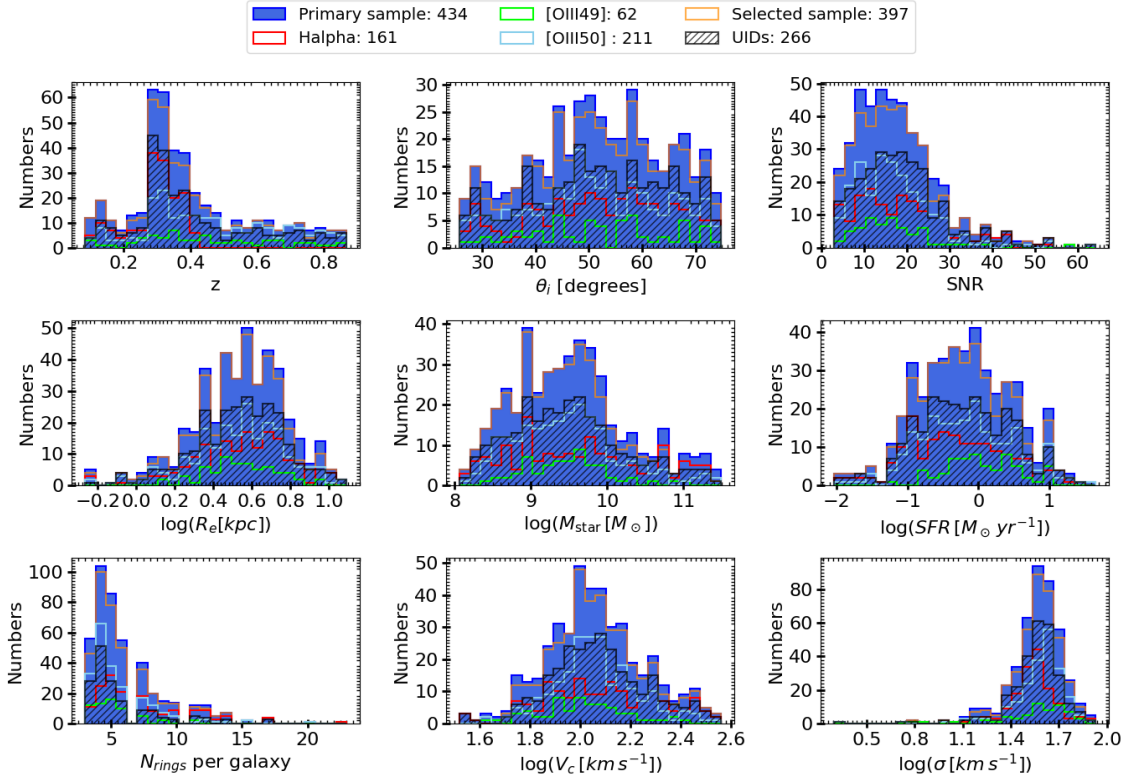


Figure 2. Distributions of key galaxy properties for the full sample used in this study. Each panel shows histograms for the primary sample (blue; 434 galaxies) and subsets based on available emission line measurements: $H\alpha$ (red; 161), $[\text{OIII}]\lambda 4969 \text{ \AA}$ (green; 62), and $[\text{OIII}]\lambda 5008 \text{ \AA}$ (sky-blue; 211). The kinematically selected sample (397) shown by orange histograms, and the black hatched histogram shows the Unique IDs (266) in this sample. Panels show (from left to right, top to bottom): redshift (z), inclination angle (θ_i ; degrees), integrated signal-to-noise ratio (SNR), effective radius R_e (kpc), stellar mass (M_{star} ; M_{\odot}), star formation rate (SFR; $M_{\odot} \text{ yr}^{-1}$), number of resolution elements (N_{rings} per galaxy), circular velocity computed at R_{opt} (V_c ; km sec^{-1}), and velocity dispersion (σ ; km sec^{-1}). The final kinematic sample and UIDs are representative of the primary sample in all fundamental properties, confirming the absence of any selection biases in the working sample.

defined following a secondary selection applied after the kinematic modelling, as described in Section 2.3.

In Figure 2, we present the distribution of key physical and morphological properties of our primary sample. Within this primary sample, we select galaxies with brightest lines for kinematic modelling: 161 using $H\alpha$, 62 using $[\text{OIII}]:4969$, and 211 using $[\text{OIII}]:5008$. The redshift range of the sample extends from $z = 0.1 - 0.85$, with $H\alpha$ predominantly probing the lower-redshift regime ($z \approx 0.1 - 0.4$), while the $[\text{OIII}]$ lines are prominent across whole redshift range. As illustrated in Figure 2 and mentioned above, our selection criteria ensure robust coverage in SNR, inclination, and stellar mass. The resulting sample spans a wide range of effective radii ($R_e = 0.5 - 10 \text{ kpc}$) and star-formation rates ($\text{SFR} = 0.01 - 32 M_{\odot} \text{ yr}^{-1}$), making it well-suited for disk galaxy population study at intermediate redshifts.

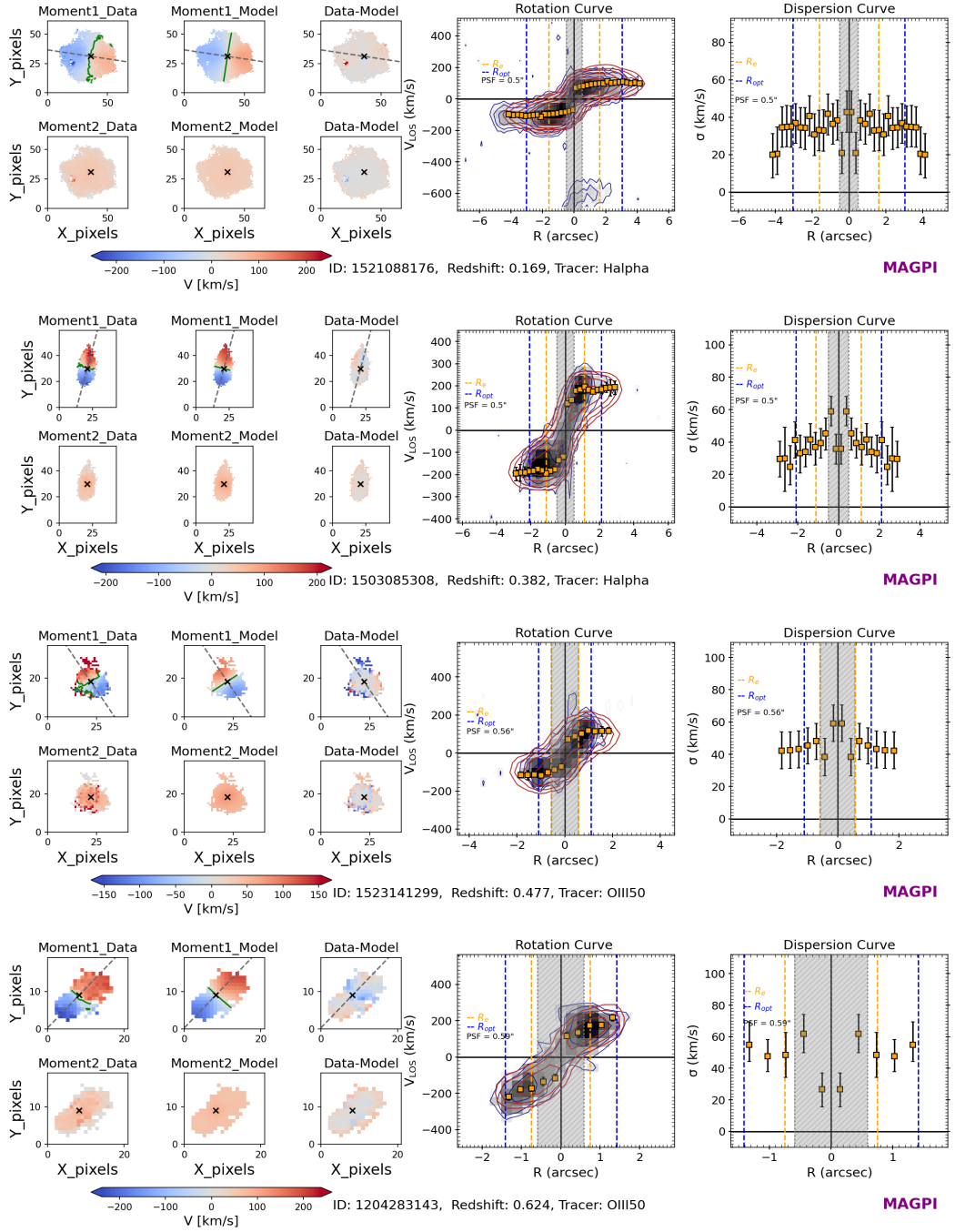


Figure 3. Examples of kinematic modelling outputs. *Row 1 & 2, Columns 1–3:* moment-1 and moment-2 maps data, best-fit model, and residuals, respectively. The grey dashed line indicates the position angle, the black cross marks the central (x, y) position, and the green line denotes the plane of rotation. *Column 4:* major axis position-velocity diagram, where the black shaded area with blue contours represents the data, red contours show the model, and orange squares with error bars indicate the best-fit line-of-sight rotation velocity derived by 3DBarolo. The yellow and blue vertical dashed lines mark the effective radius (R_e) and optical radius ($R_{\text{opt}} = 1.89 R_e$), respectively. *Column 5:* velocity dispersion profile as a function of radius. Error bars on the rotation and dispersion curves correspond to 1σ uncertainties. The PSF size is shown by gray hatched shaded region.

2.2 Forward modelling of the data-cubes

We conduct a comprehensive gas kinematics analysis of the MAGPI dataset using the 3D forward modelling approach implemented in 3DBarolo [84].⁴ The main advantages of modeling datacubes with 3DBarolo are that (1) it allows us to reconstruct the intrinsic kinematics in three spatial and three velocity components for given initial guesses that define the kinematics and geometry of a galaxy; (2) the 3D projected modeled datacubes are compared to the observed datacubes in 3D space; (3) it simultaneously incorporates instrumental and observational uncertainties (e.g., spectral smearing and beam smearing) in 3D space. This three-fold approach of deriving kinematics is designed to overcome the observational and instrumental biases faced in high- z observations/studies. In contrast, conventional 2D kinematic modelling derives velocity maps or rotation curves first and then attempts to correct for those biases a posteriori; this is less reliable for distant galaxies that have small angular sizes and moderate SNR [for more details see 48, 85].

Following our methodology in GS25, we optimize key gas geometrical parameters (central position, inclination, and position angle) using a custom optimization function that runs atop 3DBarolo. This function minimizes residuals between model and data while penalizing *non-finite* or *zero elements* in datacube array, and is solved via the Nelder-Mead algorithm (`scipy.optimize`). As demonstrated in GS25, this approach effectively overcomes limitations of photometric geometrical parameters, which often poorly trace gas kinematics at higher redshifts due to morphological misalignments between stellar and gas components [see also 70, 86]. The detailed implementation, assumptions, and limitations of this technique are described in GS25 (Section 3.1 and Appendix A).

In Figure 3, we present representative examples of the kinematic modelling for MAGPI galaxies across various redshifts and emission line tracers. The left panels display the observed gas rotation velocity (moment 1) and velocity dispersion (moment 2) maps, alongside the corresponding best-fit models and residuals (data minus model). The residual maps are generally lie on and around zero, indicating an excellent agreement between the data and the models. Similarly, the central panels show that the position-velocity diagrams along the major axis exhibit a strong overlap between the observed data and the best-fit models. These results demonstrate the high quality of the kinematic fits and underscore the effectiveness of our modelling framework in recovering the intrinsic galaxy kinematics—including the radial dispersion velocity profiles illustrated in the right panels—while accurately accounting for beam smearing and other observational effects. We note that the first point in the receding and approaching arms of rotation and dispersion curves are excluded from further analysis, as they fall within the region where 3DBarolo is unable to reliably model the kinematics (for details see [84, 85]).

2.3 Final sample

To summarize the final sample selection, it is crucial to recall that the primary selection of galaxies for kinematic modelling was based on the following criteria: (1) confirmed spectroscopic redshift and detection of either (or all) of these emission lines: $H\alpha$ (6563 Å), [OIII] (4969 Å), and [OIII] (5008 Å), (2) inclination angles within the range of $25^\circ \leq \theta_i \leq 75^\circ$, (3) $S/N > 3$, and (4) $\log(M_{\text{star}} [M_\odot]) = 8 - 11.5$. This primary selection yielded 434 galaxies that lie within 3σ range of [83] star-forming main sequence, as shown in Figure 1, with the distribution of their physical properties illustrated in Figure 2.

⁴We use latest version of 3DBarolo, which is publicly available at <https://editeodoro.github.io/Bbarolo/>

Following the kinematic modelling process (Section 2.2), we applied secondary selection criteria to remove galaxies with unreliable or insufficient kinematic constraints. Under this criteria, galaxies were excluded if they met the following conditions: (1) 3DBarolo+ optimization did not succeed, indicating unreliable optimized parameters such as PA or central coordinates; (2) No mask was created, implying 3DBarolo’s failure to mask true emission due to either a merger or moderate signal-to-noise; (3) $R_{\max} < \text{PSF}$, indicating 3DBarolo’s inability to create rings and hence fails to produce kinematic models; (4) $R_{\max} = \text{PSF}$, in this case resulting kinematic models provide only two to three velocity measurements in rotation curves, deemed insufficient for robust dynamical modelling. For further details and justification of the kinematic modelling quality control criteria, we refer the reader to GS25.

After applying the secondary selection criteria, we found that 18 galaxies failed to converge during the 3DBAROLO optimization, 9 galaxies lacked sufficient emission to construct a reliable mask, 6 galaxies exhibited $R_{\max} < \text{PSF}$, and 4 galaxies had $R_{\max} = \text{PSF}$. Consequently, the kinematically selected sample consists of 397 galaxies, as shown by the orange histograms in Figure 2. Within this sample, 23 galaxies have kinematic measurements from all three emission lines, 1 galaxy from $\text{H}\alpha$ and $[\text{OIII}]\lambda 4969$, 54 from $\text{H}\alpha$ and $[\text{OIII}]\lambda 5008$, and 26 from $[\text{OIII}]\lambda 4969$ and $[\text{OIII}]\lambda 5008$. Additionally, 67, 6, and 89 galaxies are uniquely detected in $\text{H}\alpha$, $[\text{OIII}]\lambda 4969$, and $[\text{OIII}]\lambda 5008$, respectively. The final sample therefore includes 266 unique star-forming galaxies, hereafter (and in the plots) referred to as UIDs, which are highlighted with stars in Figure 1 and represented by the black hatched histograms in Figure 2. For statistical robustness, however, all 397 kinematic measurements are included in the subsequent analysis, details are discussed in Section 2.4.

2.4 Rotation curve robustness across emission lines

When comparing rotation curves derived from different emission lines, it is important to consider that each line may trace gas with different kinematic behaviours, potentially including non-circular motions (e.g., outflows or turbulent broadening). For instance, in star-forming disc galaxies, higher-ionisation lines such as $[\text{OIII}]$ may exhibit broader wings or blue-shifted components driven by stellar or AGN feedback (see e.g. [87]). If an emission line includes a significant outflow component, the derived rotation velocity and velocity dispersion may be biased, thereby affecting the subsequent mass decomposition and inferred DM fraction. In contrast, lower-ionisation lines such as $\text{H}\alpha$ are often more closely associated with the rotationally supported disc plane and may provide a cleaner tracer of the underlying gravitational potential (e.g. [88]).

At the same time, the use of multiple emission lines, $\text{H}\alpha$, $[\text{OIII}]\lambda 5008$, and $[\text{OIII}]\lambda 4960$, provides key advantages. First, it allows us to build a larger and a broad redshift range sample. Especially, when working at high-redshift where $\text{H}\alpha$ lie outside the MUSE spectral range, $[\text{OIII}]$ remains accessible; hence, become essential for tracing ionized gas kinematics at high- z . Second, the spatial extent of the emission varies between lines: $[\text{OIII}]\lambda 4960$ is typically detected in the more central regions compared to $\text{H}\alpha$ and $[\text{OIII}]\lambda 5008$, thus providing complementary constraints on the inner rotation curve. Our final sample includes 23 galaxies for which all three emission lines are available, and 81 galaxies with either of the two combinations of emission lines as mentioned in Section 2.3.

As demonstrated in Figure 4, the subset of galaxies with all three emission lines show that the rotation curves overlap within uncertainties and that no systematic residuals remain. Moreover, their circular velocities within R_e and R_{opt} are consistent within 0.05 dex. That is, these different emission lines, despite variations in line strength and ionization potential,

consistently trace the same underlying gravitational potential ($\propto V_c^2$). This agreement indicates that any (or all) of these lines can be reliably used to derive gas kinematics and the DM fractions at all redshifts probed in this work. Nonetheless, we caution that differential line-broadening or hidden non-circular motions could still introduce additional systematic uncertainties. We verify consistency for the subset of galaxies with both $\text{H}\alpha$ and $[\text{OIII}]\lambda 5008$ by comparing their rotation curves and their circular velocities at different radii, yet fully quantifying any residual bias remains challenging without higher spectral resolution and advanced kinematic modelling tools, as highlighted in Section 3.3.

Finally, to prevent multiple occurrences of the same galaxy in the statistical representation of the dark matter fraction trends, we assign a single representative value to galaxies with measurements from more than one emission line. For such galaxies, the dark matter fraction is computed using an inverse-variance (error-weighted) average:

$$x_i^{\text{rep}} = \frac{\sum_{j=1}^N x_i^{(j)} / (\sigma_i^{(j)})^2}{\sum_{j=1}^N 1 / (\sigma_i^{(j)})^2}, \quad (2.2)$$

where $x_i^{(j)}$ denotes the dark matter fraction of the i -th galaxy measured from the j -th emission line, $\sigma_i^{(j)}$ is the corresponding measurement uncertainty, and N is the number of available emission-line measurements for that galaxy. The propagated uncertainty on the representative value is given by

$$\sigma_i^{\text{rep}} = \sqrt{\sum_{j=1}^N \frac{1}{(\sigma_i^{(j)})^2}}. \quad (2.3)$$

This procedure ensures that each galaxy contributes a single statistically independent data point to the population-level analysis while optimally incorporating information from multiple emission-line tracers.

3 Method

In this section, we outline the methodology used to derive DM fractions in our galaxy sample following the same approach presented in GS25. Firstly, we perform a mass decomposition method for the stellar disk and bulge, as well as gas disk components. Then, we introduce the formalism used to estimate the DM fraction.

3.1 Mass modelling of rotation curves

To disentangle the baryonic components and estimate the DM fraction from the rotation curves, we first applied the pressure support correction, a method introduced in [48] and briefly described in Appendix A. Pressure support corrected rotation curves fairly provide us with intrinsic total circular velocity profile ($V_c(R)$) of the system. This $V_c(R)$ is composed of the contribution of baryons (stars and gas) and DM, which gives us total dynamical mass of the system:

$$V_c^2(R) = \frac{GM_{\text{dyn}}(R)}{R}, \quad (3.1)$$

where,

$$M_{\text{dyn}}(R) = M_{\text{Disk}}(R) + M_{\text{bulge}}(R) + 1.33 M_{\text{HI}}(R) + M_{\text{H}_2}(R) + M_{\text{DM}}(R) \quad (3.2)$$

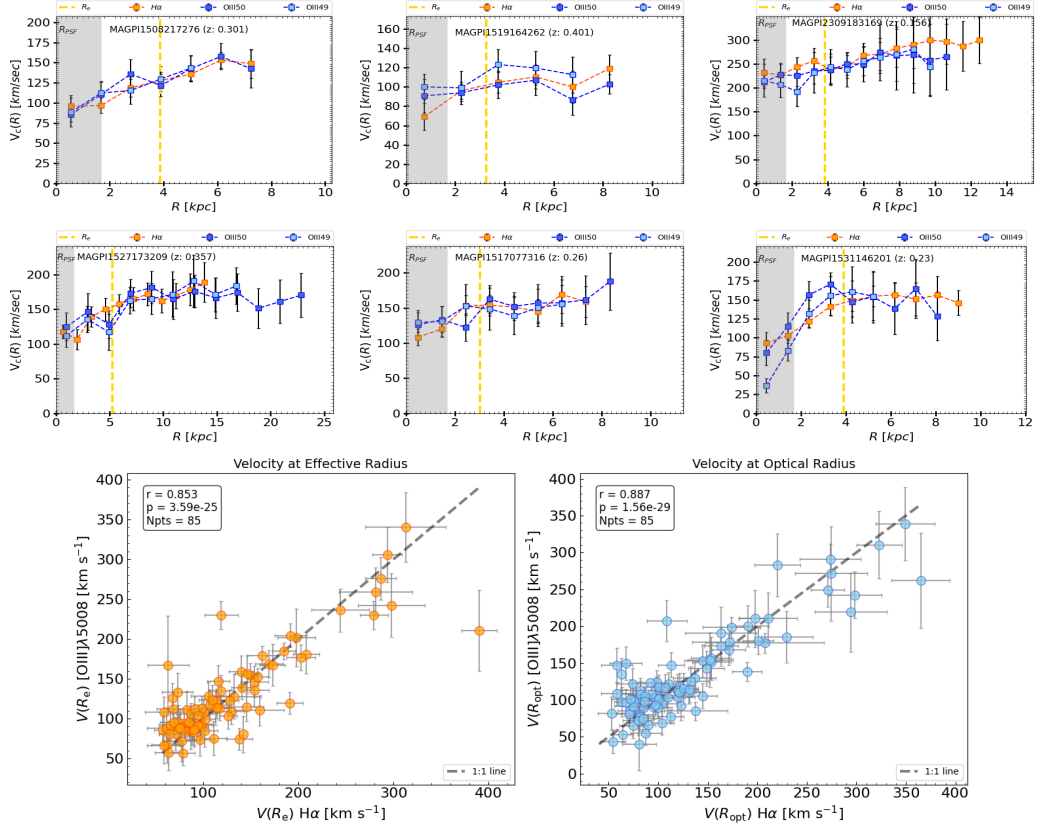


Figure 4. Row 1-2: Example rotation curves derived from multiple emission lines. The circular velocity profiles are shown for H α (orange), [O III] λ 5008 (light blue), and [O III] λ 4960 (dark blue). The vertical yellow dashed line indicates the effective radius R_e , and the shaded gray region marks the beam-smearing-affected region R_{PSF} . Row 3: Comparison of velocities traced using H α and [O III] λ 5008 within effective radius and optical radius, left and right panels, respectively.

where, the total dynamical mass ($M_{\text{dyn}}(R)$) is decomposed into the contributions from the stellar disk $M_{\text{Disk}}(R)$, bulge $M_{\text{bulge}}(R)$, atomic gas (HI) $M_{\text{HI}}(R)$, molecular gas (H₂) $M_{\text{H}_2}(R)$, and DM $M_{\text{DM}}(R)$. Here, G is the gravitational constant and the factor 1.33 in M_{HI} accounts for the Helium contribution in neutral gas. In molecular gas we do not multiply by the Helium factor because it is incorporated into the molecular gas scaling relation of [89] discussed in Appendix B. This formulation allows us to compute the DM mass distribution (and fraction) by removing the contribution of baryons from the total dynamical mass. In the following sections, we present an approach to model the aforementioned components from pressure support corrected rotation curves. We note that the circular velocity measured at R_{opt} —where the rotation curve is typically flat—is adopted as the characteristic circular velocity (V_c) of a galaxy.

Stellar and gas disk: As demonstrated in Section 2, the MAGPI sub-sample analysed here lies on and around the the star-forming MS. While there is some structural diversity on the MS, the majority of galaxies have been shown to be well described by discs [e.g., 33, 90]. Moreover, as shown in Figure 13, the galaxies in our sample are rotationally supported systems, i.e., consistent with late-type spirals on the main sequence that host well-ordered

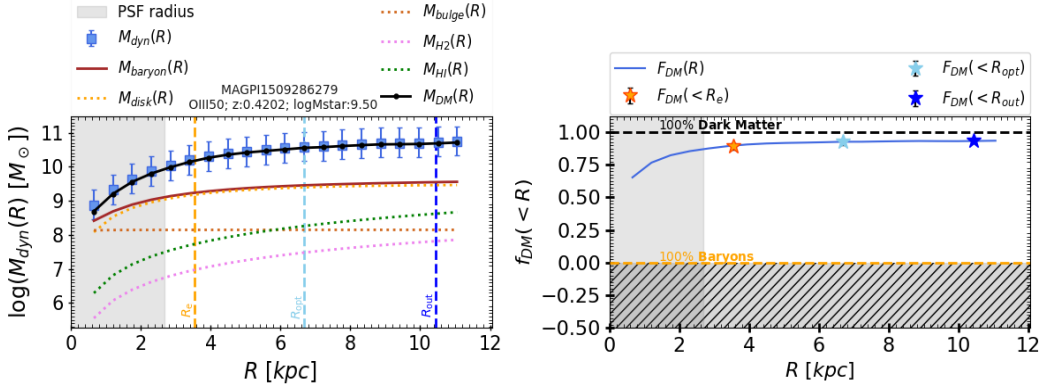


Figure 5. Mass decomposition properties of the MAGPI galaxy sample. *Left panel:* cumulative mass profiles for an example galaxy (MAGPI1509286279, $z = 0.4202$, $\log(M_{star} M_{\odot}) = 9.50$). The total dynamical mass (blue squares), baryonic mass (red line), stellar disk mass (orange line), bulge mass (brown line), atomic gas mass (green dotted line), molecular gas mass (pink dotted line), and DM mass (black line) are shown. The vertical gray shaded area and dashed lines in orange, sky blue, and blue indicate the PSF, effective radius (R_e), optical radius (R_{opt}), and outer radius (R_{out}), respectively. *Right panel:* Corresponding DM fraction as a function of radius. The solid blue line shows the cumulative DM fraction $f_{DM}(< R)$, with the horizontal black and orange dashed lines indicating 100% DM (top) and 100% baryons (bottom), respectively. Stars indicate the DM fraction within the R_e (orange), R_{opt} (cyan), and R_{out} (blue).

stellar disks [e.g., see 91]. Therefore, in modelling the disk component, we assume that the stellar and gas mass distributions follow an exponential profile, as described by the Freeman disk [92]:

$$M(R) = M_{-}^{\text{tot}} \left(1 - \left(1 + \frac{R}{R_{\text{scale}}} \right) \exp \left(-\frac{R}{R_{\text{scale}}} \right) \right) \quad (3.3)$$

where, M_{-}^{tot} and R_{scale} are the total mass and the scale length of the different baryonic components (stars, H₂, and HI). For example, if we work with stellar component $R_{\text{scale}} = R_D$ and $M_{-}^{\text{tot}} = M_{star}^{\text{tot}}$. We note that the total stellar mass is estimated using SED fitting and the total atomic and molecular gas masses are estimated using scaling relations, for details see Section 2 & Appendix B, respectively. The stars are assumed to be distributed within the stellar disk radius (i.e., in this case $R_{\text{scale}} = R_D = 0.59 \times R_e$) known from photometry, discussed in Section 2. The molecular gas is generally distributed outward through the stellar disk (up to the length of the ionized gas R_{gas}); therefore, we take $R_{H2} \equiv R_{\text{gas}}$. We estimate the gas scale length R_{gas} by fitting the H_{α} surface brightness, see [51, see Appendix-C]. Moreover, studies of local disk galaxies have shown that the surface brightness of the HI disk is much more extended than that of the H₂ disk [93, see their Fig. 5]; see also [94] and [95]. Therefore, we assume $R_{HI} = 2 \times R_{H2}$, which is a rough estimate, but still reasonable, considering that at high- z very little information is available on the M_{HI} (or M_{H2}) surface brightness distribution.

Stellar bulge: Accurately modelling the stellar bulge component is essential for galaxies at intermediate redshifts, as many star-forming galaxies exhibit bulge signatures that can substantially affect the inner mass distribution and gravitational potential [96–98]. Neglecting

the bulge contribution may lead to overestimation of the DM fraction in the central regions. Therefore, we provide first order approximation to model the bulge mass distribution. A detailed bulge-disk decomposition will be presented in a follow up work of Mauro et al. and Thater et al. (in preparation). In this work, we use an analytic Hernquist profile [99], which provides a realistic description of spherical bulges, in which the enclosed mass as a function of radius is given by:

$$M_{\text{bulge}}(r) = M_{\text{bulge}} \frac{R^2}{(R + R_{\text{bulge}})^2}, \quad (3.4)$$

where M_{bulge} is the total bulge mass and R_{bulge} is the bulge scale radius. The total bulge mass is estimated using bulge-to-total stellar mass ratio of star-forming main-sequence galaxies given by [97], which has an average scatter of less than 0.1 dex. The scale radius is computed following the empirical relation from [100], which links bulge mass to effective radius as:

$$R_{\text{bulge}} = 10^{0.84 \log_{10}(M_{\text{bulge}}) - 8.81}, \quad (3.5)$$

where R_{bulge} is in kiloparsecs and M_{bulge} in solar masses. The relation has an intrinsic scatter of 0.22 dex in the R_{bulge} direction. While this relation was calibrated for local bulges, it remains a reasonable approximation for star-forming galaxies at $0 < z \lesssim 1.0$, as studies have shown that the structural properties of bulges, including size–mass relations, evolve only mildly at these redshifts [e.g., 101, Fig. 11]. Therefore, applying this relation provides a physically motivated, first-order, estimate of the bulge scale radius in the absence of direct bulge size measurements at intermediate-redshifts.

3.2 DM fraction

The DM fraction is computed by comparing the total dynamical mass to the baryonic mass budget within a given radius. Following Equations 3.3, & 3.4 baryonic mass within radius R is calculated as:

$$M_{\text{bar}}(r) = M_{\text{Disk}}(R) + M_{\text{bulge}}(R) + M_{\text{H}_2}(R) + 1.33 M_{\text{HI}}(R), \quad (3.6)$$

The DM mass enclosed within R is then:

$$M_{\text{DM}}(R) = M_{\text{dyn}}(R) - M_{\text{bar}}(R).$$

Finally, the DM fraction is given by:

$$f_{\text{DM}}(R) = \frac{M_{\text{DM}}(R)}{M_{\text{dyn}}(R)}. \quad (3.7)$$

In Figure 5, the left panel shows cumulative mass profiles for a representative galaxy, separating the contributions from the stellar disk, bulge, atomic and molecular gas, and dark-matter halo, as derived from Equations 3.6–3.7. The cumulative dynamical mass closely follows the total baryonic+DM profile, with DM dominating at most radii in this example (although this is not universally the case for every galaxy in the sample). The right panel plots the cumulative dark-matter fraction versus radius, revealing a monotonic increase that marks the transition from a baryon-dominated center to a dark-matter-dominated halo. Together, these panels illustrate our mass-decomposition method and provide a concrete example of how we estimate dark-matter fractions across the full sample. We note that our estimates of the DM fraction are limited up to the optical radius ($R_{\text{opt}} = 1.89 \times R_e$), as the outermost radius ($3 \times R_e$) is not uniformly covered across the full sample. For clarity, we define the region within R_e as the *inner region*, and region from R_e to R_{opt} as the *outskirts*. The circular velocity measured at R_{opt} is denoted as V_c .

3.3 Uncertainties & limitations

Uncertainties on the velocity measurements are provided by 3DBAROLO using Monte Carlo Markov Chain (MCMC) sampling. Morphological parameters (e.g., the effective radius), stellar masses and star-formation rates likewise incorporate statistical uncertainties derived via MCMC sampling. The statistical uncertainties on bulge mass and bulge scale length are fixed to 0.01 dex and 0.22 dex, respectively. For each galaxy, the fraction of DM is computed by propagating all relevant uncertainties via a Monte Carlo sampling with 10000 realizations. In each realization the input values (velocity, stellar & gas mass, bulge mass, SFR, and scale lengths) are randomly drawn from their respective error distributions, and systematic uncertainties (such as those on SFR estimates ~ 0.1 dex) and the intrinsic scatter of gas-mass scaling relations are included (~ 0.3 dex for both HI and H₂, independently). Thus the derived distribution of dark-matter fraction encapsulates both statistical and systematic offsets. To derive the average dark-matter fraction of the sample, we compute both the weighted mean and the median. Uncertainties on these average values are estimated via bootstrap resampling and are reported as the 68% confidence intervals.

We emphasize that the study of DM fraction at high- z is very challenging and requires significant refinements in both baryonic constraints and kinematic modeling. For example, SED fitting techniques, which are commonly used to estimate stellar masses and SFRs, exhibit substantial offsets from each other [102, 103]. These discrepancies not only lead to larger uncertainties in stellar masses and SFRs, but also impact the gas mass scaling relations. For instance, [89], molecular gas mass scaling relation, uses the [83] main-sequence relation (M_* -SFR plane). At $z \sim 0.1$, the [83] main sequence differs from [104] by ~ 0.4 dex, and at $z \sim 1$, it is ~ 0.25 dex off from the 3DHST study [105]. At higher redshifts, this offset is not yet quantified. Therefore, the systematic offset and observed scatter in gas scaling relation, which rely on main-sequence relation is complex to accurately quantify, and beyond of the scope of this study.

Due to the lack of direct measurements of HI gas at high redshifts ($z > 1$), accurate gas scale length and masses at $z > 1$ are still unavailable. At $z \leq 1$, HI mass scaling relations are derived using stacking analyses, as current observing facilities only allow HI signal detection without resolution [106]. Hence, it gives only global gas mass but scale length is still impossible to measure. Moreover, these HI scaling relations are general and not specifically for star-forming ‘disk-like’ galaxies. That is, we can use them as a first order approximation, but they are not accurate. Refining HI mass and scale length will require future observations from the Square Kilometer Array [e.g., 107, 108, and references therein].

Moreover, current kinematic modeling techniques are limited by their inability to fully account for non-circular motions, gas inflows, and outflows [109]. As a result, achieving accurate estimates of the total dynamical mass remains challenging. Additionally, the stellar bulge is typically unresolved; thus, its mass and scale length are inferred from empirical scaling relations [97, 100], each introducing their own intrinsic scatter.

Addressing aforementioned issues will require very high-resolution large galactic-scale surveys at high redshifts, which are currently not feasible even in optical and near-infrared astronomy. Further progress might only be possible with the Extremely Large Telescope and Square Kilometer Array. Nevertheless, given the best possible information available on baryonic content, observed kinematics, and their uncertainties, we present conservative DM fraction estimates (and their uncertainties) to the best of our abilities. However, we acknowledge that these findings require further refinement, which will be achieved as the field progresses.

4 Results & discussion

In this section, we examine the relationship between the dark matter, baryonic content, and halo assembly properties. We also present the DM evolution with cosmic time. Specifically, we analyze the scaling relations of the DM fraction measured within the effective radius (R_e , refer to as inner region) and the optical radius (R_{opt} , refer to as outskirts). We include only galaxies for which the radius of interest (R_e or R_{opt}) exceeds the PSF FWHM, to ensure reliable measurements. As a result, DM fraction within R_e and R_{opt} is presented for 181 and 246 galaxies, respectively.

4.1 Dark matter dynamics: scaling f_{DM} with V_c

In Figure 6, we present the relationship between the DM fraction and the circular velocity of galaxies. The DM fraction is computed within R_e (inner region; left panel) and R_{opt} (outskirts; right panel). To provide a reference for the baryonic component, galaxies are color-coded by their stellar masses. The error bars reflect the full propagation of mass-model uncertainties at the 1σ level. We notice that the low-mass galaxies ($M_{\text{star}} < 10^{9.5} M_{\odot}$) are typically low-rotational-support systems ($V_c < 100 \text{ km s}^{-1}$) and exhibit a median DM fraction of $\langle f_{\text{DM}}(< R_e) \rangle = 0.7 \pm 0.1$ and $\langle f_{\text{DM}}(< R_{\text{opt}}) \rangle = 0.75 \pm 0.05$. That is, at low V_c and low stellar masses, galaxies are DM dominated as expected for low-mass systems where baryons contribute less to the overall potential. In contrast, high-rotational-support systems ($V_c > 100 \text{ km s}^{-1}$) are predominantly associated with intermediate- to high-mass galaxies ($10^{9.5} \leq M_{\text{star}} [M_{\odot}] \leq 10^{11.5}$). In these systems, the DM fraction within R_e decreases significantly with increasing stellar mass, while the decline in the outskirts (R_{opt}) is modest. We show this quantitatively in Figure 7, where we notice that the DM fraction for high-rotational-support systems is reduced by approximately 40% in the inner regions, compared to only about a 10% reduction in the outskirts (see the blue median-fit compared to orange). This relatively large change in f_{DM} in the inner regions of galaxies likely reflects the influence of baryonic feedback processes and the central concentration of baryons relative to the DM distribution.

These findings are consistent with those observed in local disk galaxies [e.g., 13, 38], as well as in high- z star-forming, disk-like galaxies [51, 52], where the authors demonstrated that, at fixed circular velocity, low-mass galaxies exhibit a higher DM fraction within a representative radius compared to their high-mass counterparts. Furthermore, the positions of the Milky Way, having $M_{\text{star}} = 10^{10.78} M_{\odot}$ [110, and ref. therein] and Andromeda, with $M_{\text{star}} = 10^{11.01} M_{\odot}$, [111, and ref. therein] lie within the locus of the most massive ($\log(M_{\text{star}}, M_{\odot}) = 10.5 - 11.5$) MAGPI galaxies. That is, their f_{DM} values are broadly consistent with the local massive spiral galaxies. Although, the scatter in f_{DM} at fixed V_c suggests the diversity in baryon-to-DM ratios among galaxies with similar rotation velocities—potentially reflecting differences in formation histories, feedback mechanisms, or baryonic concentrations—approximately 25% of this scatter can be attributed to the measurement uncertainties in f_{DM} . This scatter could also be a consequence of “progenitor bias”, as the progenitors of the low stellar mass galaxies drop out of the sample at high redshift [e.g., see also 112, 113]. The absence of a sharp transition and the continuous trend across V_c suggest that the DM fraction is primarily connected with stellar mass and surface density (see Section 4.2) rather than by circular velocity alone.

Furthermore, we remark that a very small subset of galaxies in Figure 6 appear to exhibit negative DM fractions (i.e., $f_{\text{DM}} < 0$) within R_e (3 galaxies) and R_{opt} (1 galaxy), particularly at the high-mass end. These unphysical values suggest that the baryonic mass,

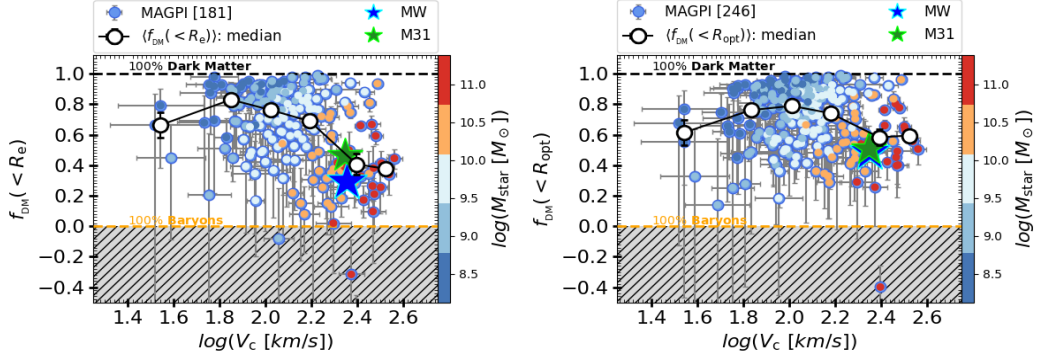


Figure 6. DM fraction (f_{DM}) as a function of circular velocity (V_c). The left and right panels shows the DM fraction within the effective radius (R_e) and optical radius (R_{opt}), respectively. In both panels, individual galaxies are color-coded by stellar mass (M_{star}). The white circles with error bars represent the median $\langle f_{\text{DM}} \rangle$ values in bins of V_c . The errors on the datasets (individual and average) are 68% confidence intervals. The positions of the Milky Way (MW; blue star, [110]) and Andromeda (M31; green star, [111]) are shown for comparison with local massive disk galaxies. Horizontal black and orange dashed lines indicate the 100% DM and 100% baryons limits, respectively. The gray hatched region corresponds to unphysical negative DM fractions. These panels show that the majority of galaxies are DM dominated and illustrate the dependence of the DM content on galaxy mass and rotation velocity, with a clear increase in f_{DM} at lower M_{star} and V_c .

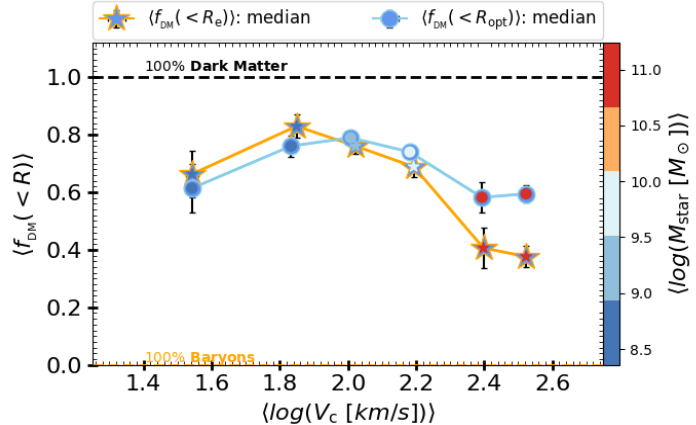


Figure 7. Averaged DM fraction ($\langle f_{\text{DM}} \rangle$) within the effective radius (stars) and optical radius (circles), computed in bins of circular velocity (V_c). Each $\langle f_{\text{DM}} \rangle$ value is color-coded for median stellar mass obtained in the corresponding velocity bin. These results demonstrate that, in high-rotation-support systems compared to low-rotation-supporters, the DM fraction within the effective radius is reduced by approximately 30-40% (including errors) relative to its value at the optical radius, whereas the reduction within the optical radius, for such systems, is limited to about 10%.

inferred from a combination of photometric SED fitting and gas scaling relation, exceeds the total dynamical mass derived from rotation curves.⁵ While such discrepancies could

⁵We define a negative DM fraction as unphysical because the total observed dynamical mass (inferred from

arise from systematics in the kinematic modelling, we attribute the bulk of this effect to systematics in stellar mass estimation. Specifically, recent comparisons with stellar masses derived from full-spectral fitting (see Appendix C) indicate that broad-band SED-fitting based stellar masses tend to be systematically higher (see Figure 14). Applying full-spectral fitting (Poci et al. in prep.) significantly reduces or eliminates the population of “dark matter-deficient ($f_{\text{DM}} < 20\%$)” galaxies, bringing their f_{DM} values into physically plausible ranges, see Figure 14. This reinforces the robustness of our overall trends and highlights the importance of more precise stellar mass estimation in studies of DM content. We note that the full-spectral fitting stellar masses are not yet available for full sample used in this work; therefore, we adopt the photometric SED-based stellar masses as our baseline for all primary analyses presented in this study.

4.2 Dark matter dynamics: scaling f_{DM} with Σ_{bar}

Figure 8 shows the f_{DM} as a function of baryon mass surface density, measured within the effective radius (left) and out to the optical radius (right). Each point represents a MAGPI galaxy, colour-coded by stellar mass; the error bars show 1σ uncertainties. The dashed black curve indicates a power-law fit:

$$f_{\text{DM}}(< R) = 1 - 10^{\left(-0.13+0.55\left(\log \frac{\Sigma_{\text{bar}}}{[M_{\odot} \text{ kpc}^{-2}]} - \alpha\right)\right)}, \quad (4.1)$$

where Σ_{bar} is baryon mass surface density defined as $\Sigma_{\text{bar}}(< R) = \frac{M_{\text{bar}}(< R)}{\pi R^2}$, $\alpha = 8.7 \pm 0.1$ for R_e and $\alpha = 8.5 \pm 0.1$ for R_{opt} .

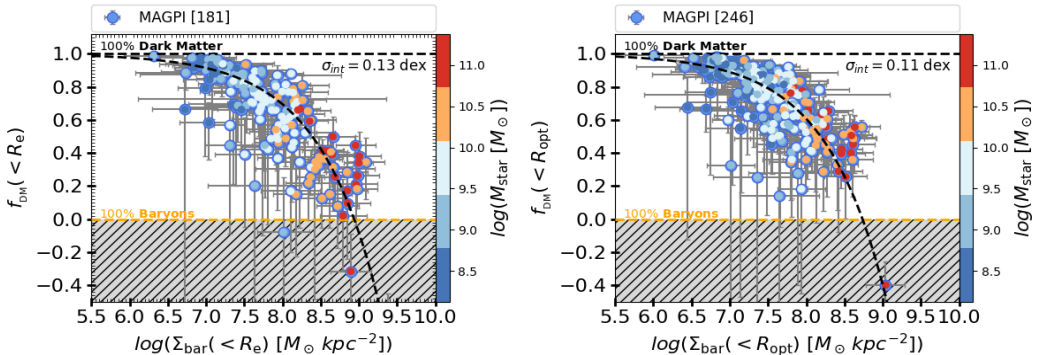


Figure 8. DM fraction (f_{DM}) as a function of baryon mass surface density (Σ_{bar}). *Left and right panels:* DM fraction within the effective radius (R_e) and optical radius (R_{opt}), respectively. In both panels, individual galaxies are color-coded by stellar mass (M_{star}). The errors on the datasets are 68% confidence intervals. The black dashed curve shows the best-fit relation, and intrinsic scatter (σ_{int}) around best-fit is printed at the top right corner. The black and orange horizontal dashed lines mark the 100% DM and 100% baryon limits, respectively. The gray hatched region corresponds to unphysical (negative) DM fractions. Both panels highlight the inverse correlation between the DM fraction and baryonic mass surface density, with lower surface density systems being increasingly DM dominated.

These results reveal a clear inverse correlation between DM fraction and baryon surface density. Galaxies with higher central baryon surface densities $\Sigma_{\text{bar}} \gtrsim 10^{8.0} M_{\odot} \text{ kpc}^{-2}$ are

rotation curves) cannot be less than the total observed baryonic mass.

more baryon-dominated in their inner regions. In contrast, systems with low baryonic surface densities $\Sigma_{\text{bar}} < 10^{8.0} M_{\odot} \text{kpc}^{-2}$ are increasingly dominated by dark matter. The low intrinsic scatter of 0.13 dex and 0.11 dex for R_e and R_{opt} , respectively, indicates that f_{DM} is tightly connected with Σ_{bar} . In comparison to high- z disk-like galaxies ($z > 0.8 - 2.2$), studied in [GS25](#), the relation presented here is relatively tight, showing factor of two lower intrinsic scatter, suggesting that the connection between baryonic surface density and DM fraction is well established at the intermediate redshifts probed by MAGPI survey at $0.1 \lesssim z \lesssim 0.85$. This comparatively tight correlation could also be due to the relatively high spatial resolution ($\sim 3\text{kpc}$) in MAGPI dataset obtained with MUSE, which wasn't the case for [GS25](#) sample ($\sim 4\text{kpc}$). Nevertheless, this tight correlation supports a scenario in which disk galaxy mass assembly—and the resulting equivalence between baryons and dark matter—is largely in place by $z \lesssim 0.85$, echoing the structural regularities (e.g., flat rotation curves) observed in nearby disk galaxies. Interestingly, our findings agree with those in the local Universe, where late-type spiral galaxies and low-surface-brightness galaxies exhibit a similar dependence of the DM content on baryonic surface density [e.g., [13, 114–116](#)]

The observed increase of Σ_{bar} with stellar mass and decreasing DM fraction in both the inner (R_e) and outer (R_{opt}) regions also support the scenario described in the introduction. In this framework, massive galaxies initially undergone more efficient gas in-fall, central condensation, and star formation, most-likely tied to the low specific angular momentum, filamentary gas accretion [[18, 24, 25, 117](#)], potentially followed by compaction of the gas that can lead to starbursts [[22, 23](#)]. This naturally leads to concentrated gas and stellar components that are characterised by high Σ_{bar} and low DM fractions.

In contrast, and according to the “downsizing” picture, lower-mass galaxies begin to assemble later, at epochs when gas accretion in a ΛCDM universe is expected to carry higher specific angular momentum [[18](#)], causing the gas to settle at larger radii. In addition, the shallower potential wells of low-mass systems make feedback more efficient at expelling baryons (see [[118](#)] for a review), thereby reducing Σ_{bar} and exacerbating the difference in the DM fraction within both R_e and R_{opt} relative to massive galaxies. In this context, the tight correlation we observe between DM fraction and Σ_{bar} can be interpreted as a direct imprint of the baryon assembly history, encapsulating how the timing, efficiency, and spatial distribution of baryonic growth regulate the inner-to-outer mass structure of star-forming disk galaxies.

4.3 Dark matter dynamics: scaling f_{DM} with z

Figure 9 shows the DM fraction as a function of redshift. The left panel presents $f_{\text{DM}}(< R_e)$, and the right panel shows $f_{\text{DM}}(< R_{\text{opt}})$. To illustrate the relationship between baryons at different redshifts, individual galaxies are colour-coded by stellar mass. To characterise the global trend, we compute the weighted mean (grey stars) and median (white circles) of f_{DM} in redshift bins. In both cases, uncertainties on the binned data points are estimated via bootstrap resampling and represent the 68% confidence interval. For details of the binning procedure, we refer the reader to [GS25](#) (Sec. 4.2).

Statistically, over the MAGPI sample redshift range $0.1 \leq z \leq 0.85$, the median DM fraction within the R_e is approximately 0.65, and the weighted mean is slightly higher (~ 0.8). At the optical radius (R_{opt}), the typical DM fraction rises to about 0.85. Given the uncertainties on the measurements, within both the R_e and R_{opt} , the data show no significant trend with redshift. This suggests that for rotation-supported systems that lie on the star-forming main sequence, the balance between baryonic and DM components within these

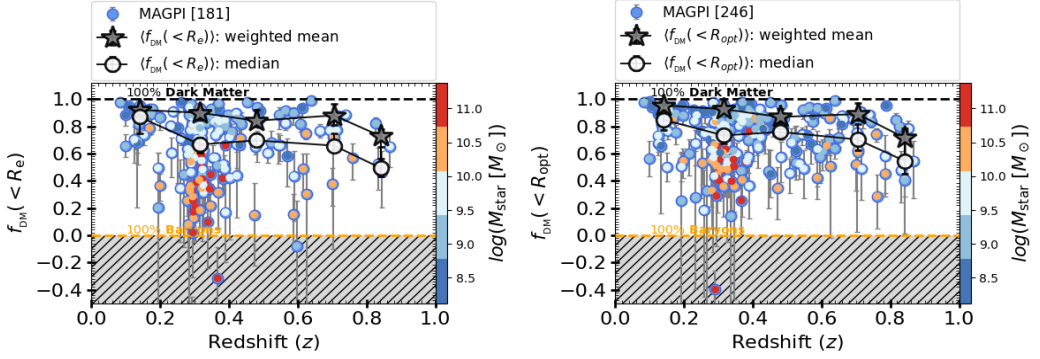


Figure 9. DM fraction (f_{DM}) as a function of redshift. *Left and right panels:* DM fraction within the effective radius ($f_{\text{DM}}(< R_e)$) and optical radius ($f_{\text{DM}}(< R_{\text{opt}})$), respectively, plotted against redshift. In both panels, individual galaxies are color-coded by stellar mass (M_{star}). Black circles and stars represent the median and weighted mean $\langle f_{\text{DM}} \rangle$ in redshift bins, respectively. The errors on the datasets (individual and average) are 68% confidence intervals. Horizontal dashed lines indicate the 100% DM (black) and 100% baryon (orange) limits, while the gray hatched region marks unphysical negative DM fractions. These panels show majority of galaxies are DM dominated and seems to have a very mild evolution in DM fraction across the redshift range probed, with substantial scatter at all redshifts.

characteristic radii was already largely in place by $z \sim 0.1 - 0.8$. The lack of significant evolution is consistent with the findings of GS25, who showed that high-redshift ($z \gtrsim 1$) star-forming galaxies typically exhibit elevated velocity dispersions and lower rotation-to-dispersion ratios, but once corrected for pressure support, their DM fractions within the inner regions are comparable to those of local disks [13, 38]. The MAGPI survey data now empirically support this result for intermediate redshifts.

The vertical scatter in $f_{\text{DM}}(< R_e)$ within each redshift bin is primarily driven by stellar mass. Consistent with above discussions, we observe that lower-mass disks ($M_{\text{star}} < 10^{9.5} M_{\odot}$) are generally more dark-matter dominated within their inner regions, whereas the massive systems ($M_{\text{star}} \geq 10^{10.0} M_{\odot}$) tend to be baryon-dominated at their centers. If a complete stellar mass range ($\log(M_{\text{star}}[M_{\odot}]) = 8.5 - 11.5$) were uniformly sampled across all redshift intervals, it is likely that this mass-dependent trend would be apparent at all redshifts. However, we do not explicitly observe this because low-mass galaxies are intrinsically difficult to detect at high redshift; those that are observed typically have lower signal-to-noise ratios, resulting in larger uncertainties in both dynamical and baryonic mass estimates, and consequently, in the inferred dark matter fractions. In contrast, the scatter due to mass is less pronounced in the outer regions, $f_{\text{DM}}(< R_{\text{opt}})$, we explore this more in Section 5 where we combine MAGPI sample with GS25 high- z sample.

The flat $f_{\text{DM}}(z)$ relation suggests that, although galactic disks have grown in stellar mass and size by a factor of ~ 2 since $z \sim 1$, the accompanying accretion of DM and the inside-out buildup of baryons have proceeded in lockstep [see also 119, and references therein]. Moreover, the substantial scatter in f_{DM} at fixed redshift and radius most-likely reflects the diversity of evolutionary pathways, including differences in gas accretion, star formation efficiency, and feedback history across the galaxy population.

4.4 Statistical relevance of various correlations

Table 1 presents the Pearson correlation coefficients (r) and associated p -values for the various scaling relations analysed in this study. Statistically, the coefficient r quantifies the strength and direction of a linear relationship: values near +1 indicate a strong positive correlation, those near -1 indicate a strong negative correlation, and values near zero indicate no significant correlation. The corresponding p -value assesses statistical significance; we remark that $p < 0.05$ is used as the threshold for a statistically robust correlation. These correlations are computed over the UIDs (including weighted values of repeated objects) for DM fraction within both R_e and R_{opt} .

Relation Name	bins	Npoints	Corr. Coeff.	p-value
V_c vs $f_{\text{DM}}(< R_e)$	-	180	-0.3590	$7.5e - 07$
V_c vs $f_{\text{DM}}(< R_{\text{opt}})$	-	245	-0.1177	0.651
Σ_{bar} vs $f_{\text{DM}}(< R_e)$	-	180	-0.7902	$< 1e - 10$
Σ_{bar} vs $f_{\text{DM}}(< R_{\text{opt}})$	-	245	-0.7091	$< 1e - 10$
M_{star} vs $f_{\text{DM}}(< R_e)$	-	180	-0.6880	$< 1e - 10$
M_{star} vs $f_{\text{DM}}(< R_{\text{opt}})$	-	245	-0.5253	$< 1e - 10$
z vs $f_{\text{DM}}(< R_e)$	-	180	-0.0255	0.7337
z vs $f_{\text{DM}}(< R_{\text{opt}})$	-	245	-0.0257	0.6892

Table 1. Correlation statistics for various scaling relations. We present Pearson correlation coefficients (r) and associated p -values for DM fraction (f_{DM}) as a function of different galaxy properties within the effective radius (R_e) and optical radius (R_{opt}). Correlations with p -value < 0.05 are considered statistically significant. Strong negative correlations are observed between f_{DM} and both Σ_{bar} and M_{star} , indicating that higher baryonic surface density and stellar mass are associated with lower DM fractions, particularly within R_e . Correlations with V_c and redshift are also evaluated.

We find strong negative correlations between f_{DM} and both baryonic surface density Σ_{bar} and stellar mass M_{star} , within R_e and R_{opt} . These relations are highly significant (all p -values $< 10^{-10}$), with r reaching below -0.5, especially in the inner regions, suggesting that galaxies with higher stellar mass and central baryonic concentration tend to have lower DM fractions in their inner regions. These findings align with the trends discussed in Sections 4.1 and 4.2. Circular velocity, V_c , exhibits a moderate negative correlation with $f_{\text{DM}}(< R_e)$ ($r = -0.31$, $p = 1.6 \times 10^{-7}$), suggesting that faster-rotating galaxies are generally more baryon-dominated in their centers compared to outskirts. In contrast, no significant correlation is found between V_c and $f_{\text{DM}}(< R_{\text{opt}})$, implying that DM remains quite constant in the outskirts regardless of rotation speed (see Section 4.1). We also observe a statistically insignificant negative correlation between redshift and f_{DM} ($r \approx -0.02$ within R_e and R_{opt}), which we have further discussed in Section 5.

5 Dark matter evolution with cosmic-time

To obtain a comprehensive view of the DM content across cosmic time ($z = 0.1 - 1.5$) for the *disk galaxy population* ($\log(M_{\text{star}} [M_{\odot}]) = 8.0 - 11.5$), we combined the MAGPI sample with high-redshift data from GS25. The latter dataset was processed and analysed using the same modelling tools, techniques, and methodology applied in this work. In Figure 10, we present combined dataset showing the trend of the DM fraction with redshift. The top-left and top-right panels show $f_{\text{DM}}(< R_e, z)$ and $f_{\text{DM}}(< R_{\text{opt}}, z)$, respectively, with individual

galaxies color-coded by their stellar mass. The bottom panel summarizes the median and weighted mean f_{DM} trends for both radii, with shaded regions representing the 68% confidence intervals. We notice that across the MAGPI redshift window the typical dark-matter fraction remains nearly constant, with $\langle f_{\text{DM}}(< R_e) \rangle \simeq 0.7$ and $\langle f_{\text{DM}}(< R_{\text{opt}}) \rangle \simeq 0.9$ (also see Figure 9). At $z \gtrsim 1$ the GS25 galaxies exhibit lower values, producing monotonic decline in $f_{\text{DM}}(< R)$ with redshift. This declining trend is most likely due to an observational bias, the so-called Tolman Dimming effect, a relativistic phenomenon in which the observed surface brightness of a celestial object diminishes as $(1+z)^2$ [120–122], making it more difficult to measure flux from fainter sources. The smaller sizes of low-mass galaxies is an additional challenge for resolving full rotation curves.

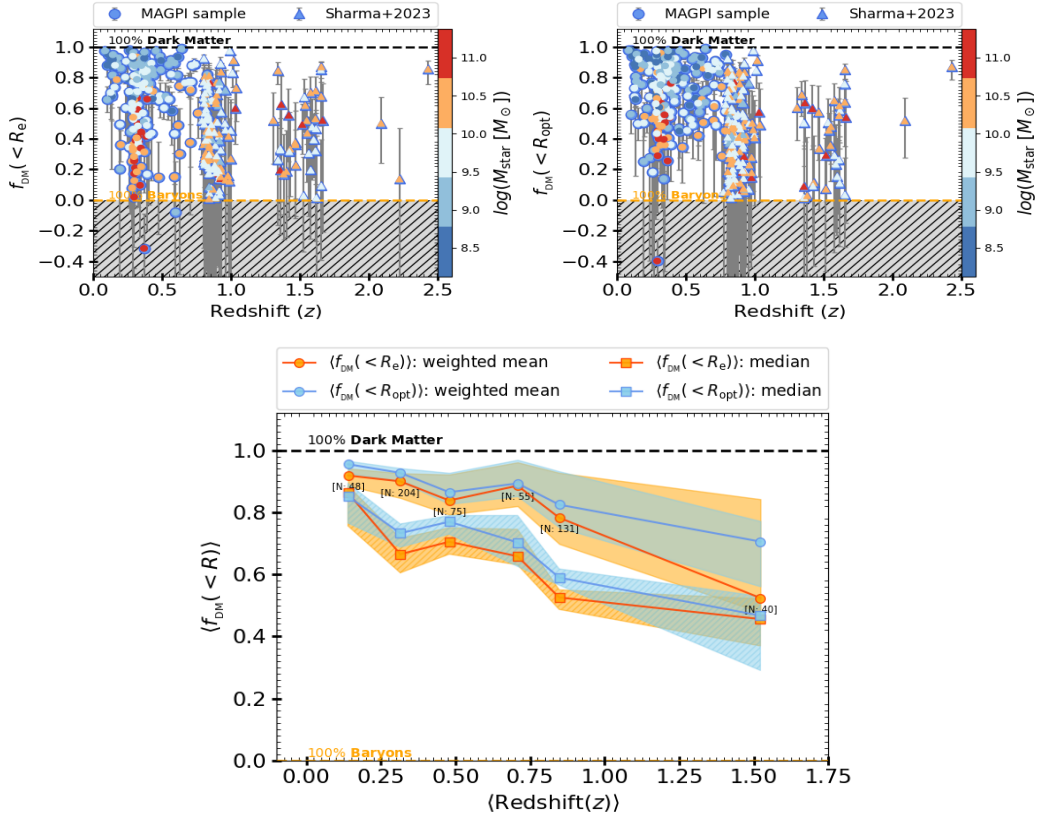


Figure 10. DM fraction (f_{DM}) as a function of redshift for the MAGPI sample and high-redshift galaxies from GS25. *top left panel:* $f_{\text{DM}}(< R_e)$ versus redshift. *top right panel:* $f_{\text{DM}}(< R_{\text{opt}})$ versus redshift. MAGPI galaxies are shown as circles while GS25 galaxies are shown as triangles, both datasets are color-coded by stellar mass. *Bottom panel:* Median values are indicated by square-connected solid lines with hatched shaded regions, and weighted mean values by circle-connected solid lines with plain shaded regions. The shaded regions are showing 1σ uncertainty, where Orange represents $f_{\text{DM}}(< R_e)$, and Blue represents $f_{\text{DM}}(< R_{\text{opt}})$.

Due to differences in targeting strategy between the KMOS and MUSE surveys, the stellar mass ranges probed are different. Therefore, to assess the impact of this observational bias on our measurements, we divide the combined galaxy sample into four stellar mass bins and examine their DM fractions within R_e and R_{opt} , as shown in Figures 11 and 12,

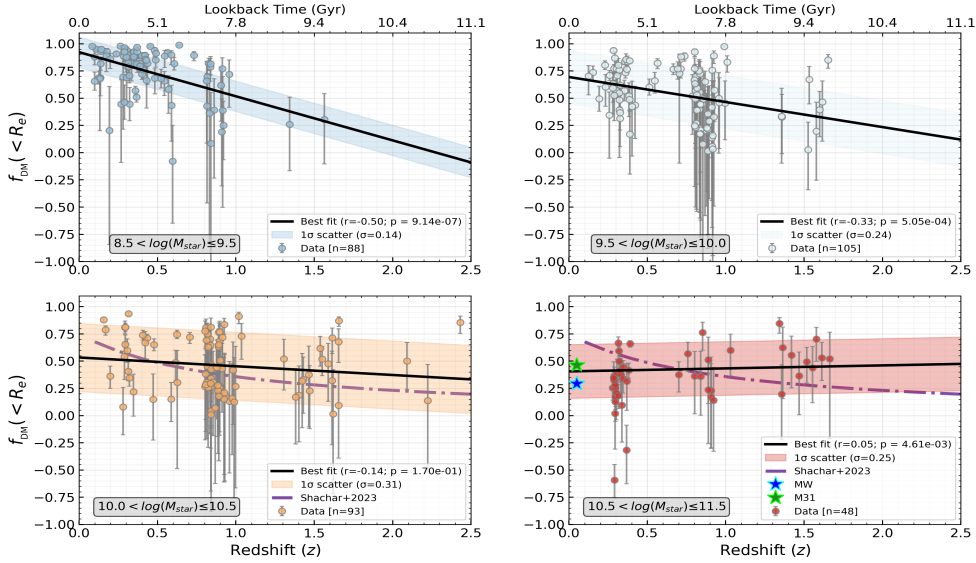


Figure 11. Redshift evolution of DM fraction within the effective radius, $f_{\text{DM}}(< R_e)$, in four stellar mass bins using the combined MAGPI+GS23 sample. Each panel corresponds to a different stellar mass bin: *Top-left*: $8.5 < \log(M_{\text{star}} [M_{\odot}]) \leq 9.5$, *Top-right*: $9.5 < \log(M_{\text{star}} [M_{\odot}]) \leq 10.0$, *Bottom-left*: $10.0 < \log(M_{\text{star}} [M_{\odot}]) \leq 10.5$, and *Bottom-right*: $10.5 < \log(M_{\text{star}} [M_{\odot}]) \leq 11.5$. The y -axis shows $f_{\text{DM}}(< R_e)$, while the x -axis denotes redshift (bottom axis) and lookback time (top axis). Each data point represents a galaxy, with error bars indicating observational uncertainties. The black lines represent best-fit linear regressions and shaded region shows the 1σ intrinsic around best-fit. Pearson correlation coefficients (r) and p -values are printed in the legend alongside best-fit. The purple dash-dotted line indicates the results from [46] for a comparable stellar mass range. For reference, the DM fractions within R_e for the Milky Way (MW) and Andromeda (M31) are shown as blue and green stars, respectively, representing massive local star-forming disk galaxies.

respectively. We find that low-mass galaxies ($\log(M_{\text{star}} [M_{\odot}]) = 8.5\text{--}9.5$) are absent at $z > 0.9$, and only a small number (~ 10) of intermediate-mass galaxies ($9.5 < \log(M_{\text{star}} [M_{\odot}]) \leq 10.0$) provide robust measurements at $z \sim 1.5$. As a result, when averaging the DM fraction above $z > 0.9$ (see Figure 10 bottom panel), the results are biased toward massive galaxies ($\log(M_{\text{star}} [M_{\odot}]) > 10$) which tend to show relatively low dark matter fractions.

Within the stellar mass range $8.5 < \log(M_{\text{star}}/M_{\odot}) \leq 10.5$, galaxies tend to show a systematic decrease in dark matter fraction with increasing redshift, both within R_e and R_{opt} . For the lowest-mass bin $8.5 < \log(M_{\text{star}}/M_{\odot}) \leq 9.5$, we find a relatively strong anti-correlation between $f_{\text{DM}}(< R_e)$ and redshift (top-left panel; $r = -0.50$, $p = 1.1 \times 10^{-6}$) and a moderate anti-correlation for $f_{\text{DM}}(< R_{\text{opt}})$ (top-left panel; $r = -0.34$, $p = 9.7 \times 10^{-5}$). In the second bin, $9.5 < \log(M_{\text{star}}/M_{\odot}) \leq 10.0$, the trends remain significant but shallower, with $r = -0.33$ ($p = 5.1 \times 10^{-4}$) for $f_{\text{DM}}(< R_e)$ and $r = -0.47$ ($p = 2.2 \times 10^{-8}$) for $f_{\text{DM}}(< R_{\text{opt}})$. For intermediate-mass systems, $10.0 < \log(M_{\text{star}}/M_{\odot}) \leq 10.5$, the correlations weaken: $r = -0.14$ ($p = 0.17$) within R_e and $r = -0.30$ ($p = 7.4 \times 10^{-4}$) within R_{opt} . In all three bins, the data at the high-redshift end ($z > 1$), display larger individual uncertainties. If we consider these trends as an evolution in dark matter fraction, then it is an empirical evidence, suggesting that the galaxies gradually accrete dark matter during their evolutionary process over the cosmic time. Additionally, the observed differences in dark matter fraction

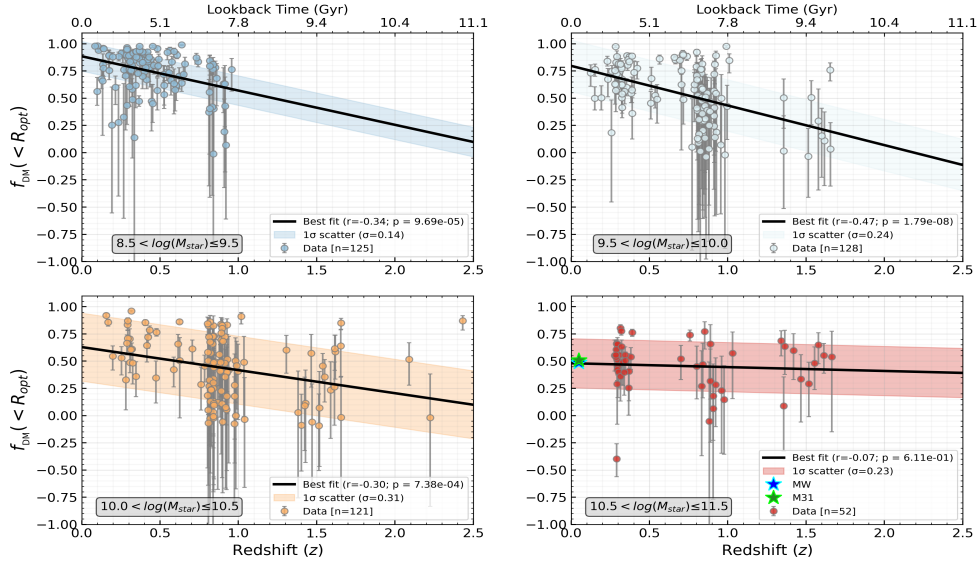


Figure 12. Redshift evolution of DM fraction within the optical radius, $f_{\text{DM}}(< R_{\text{opt}})$, in four stellar mass bins using the combined MAGPI+GS23 sample. Each panel corresponds to a different stellar mass bin: *Top-left*: $8.5 < \log(M_{\text{star}} [M_{\odot}]) \leq 9.5$, *Top-right*: $9.5 < \log(M_{\text{star}} [M_{\odot}]) \leq 10.0$, *Bottom-left*: $10.0 < \log(M_{\text{star}} [M_{\odot}]) \leq 10.5$, and *Bottom-right*: $10.5 < \log(M_{\text{star}} [M_{\odot}]) \leq 11.5$. The y -axis shows $f_{\text{DM}}(< R_{\text{opt}})$, while the x -axis denotes redshift (bottom axis) and lookback time (top axis). Each data point represents a galaxy, with error bars indicating observational uncertainties. The black lines represent best-fit linear regressions and shaded region shows the 1σ intrinsic around best-fit. Pearson correlation coefficients (r) and p -values are printed in the legend alongside best-fit. For reference, the DM fractions within R_{opt} for the Milky Way (MW) and Andromeda (M31) are shown as blue and green stars, respectively, representing massive local star-forming disk galaxies.

amplitude ($f_{\text{DM}}(\text{low } M_{\text{star}} \rightarrow \text{high } M_{\text{star}}) = 0.85 \rightarrow 0.5$) across stellar mass bins indicate that lower-mass galaxies undergo a higher degree of evolution compared to their massive counterparts (cf. GS25).

In contrast, the most massive galaxies, with $10.5 < \log(M_{\star}/M_{\odot}) \leq 11.5$, show no statistically significant evolution in dark matter fraction within R_{opt} (bottom-right panel; $r = -0.07$, $p = 0.61$), and only a mild positive trend within R_{e} (bottom-right panel; $r = 0.05$, $p = 4.6 \times 10^{-3}$), which remains small compared to the intrinsic scatter. Their mean dark matter fractions, $\langle f_{\text{DM}}(< R_{\text{e}}) \rangle \approx 0.45$ and $\langle f_{\text{DM}}(< R_{\text{opt}}) \rangle \approx 0.5$, are approximately constant over the full redshift range and comparable to those measured in massive local disks such as the Milky Way and M31. The lack of strong evolution at high masses suggests that (1) progenitors of present-day massive systems may have evolved in a manner analogous to their high-redshift counterparts, and (2) galaxies might evolve in such a way that increases in baryonic mass and growth of dark matter halo proceed in a co-regulated fashion so that the inner and outer DM fraction remains approximately constant.

Due to the targeting strategy of MAGPI, similar to [53], our sample is dominated by low mass galaxies ($M_{\text{star}} < 10^{10} M_{\odot}$; Figure 2). At these masses we find high dark matter fractions within $R_{\text{e}} \gtrsim 50\%$, consistent with [53, 123] and [46]. When all galaxies in our combined sample are considered we do not find a statistically significant trend with redshift (Figure 9 & 10) implying no evolution. However, when split by stellar mass, we see a

possible change in DM fraction evolution with mass, such that low mass galaxies show the strongest DM fraction evolution and high-mass galaxies show no-evolution. In the mass bin $10 < \log(M_{\text{star}} M_{\odot}) \leq 10.5$, our results are roughly consistent with the evolution measured in [46], although the statistical significance of this evolution in our dataset is not robust.

A flat $f_{\text{DM}}(z)$ relation, combined with the declining $f_{\text{DM}}(M_{\text{star}})$ and rising $f_{\text{DM}}(R)$ trends, supports a scenario in which the inside-out growth of stellar disks proceeds in parallel with the gradual accretion of dark matter, i.e., co-regulated build-up of baryons and dark matter in lockstep (also suggested by [119]). Some hydrodynamical cosmological galaxy simulations with strong, mass-dependent feedback and realistic halo contraction indeed find a tight co-evolution of stellar disks and DM halos. For example, IllustrisTNG results [124] show that galaxies maintain a co-evolution between baryons and DM such that their rotation curves remain flat – indicating a roughly fixed inner dark-matter fraction over time. Likewise [125] emphasize that galaxy growth proceeds in lockstep with halo growth. They note that even at the peak of star formation efficiency (halo mass $\sim 10^{12} M_{\odot}$), less than 20% of a halo’s baryons turn into stars, the rest remains in the form of gas or are expelled from halos via feedback processes. Consistent with this, [126] find in the EAGLE simulations that incorporating stellar and AGN feedback plus gradual halo response yields nearly constant baryon-to-DM fractions in both galaxy centers and outskirts over time. These simulations, looking mainly at massive galaxies, support the results of this work and suggest that baryonic and DM components co-evolve in systematic manner during disk galaxy assembly, maintaining their relative mass distribution, observed across scales and cosmic time. In a follow-up work, we will compare our results quantitatively with mock observations of aforementioned simulations.

6 Conclusions

To investigate the co-evolution of baryons and dark matter, we analyzed the dark matter fraction and its scaling relations in a sample of 266 star-forming galaxies using spatially resolved kinematic data from the MAGPI survey at intermediate redshifts ($0.1 \lesssim z \lesssim 0.85$). This work constitutes a population-level analysis of disk-like galaxies spanning a stellar mass range of $\log(M_{\text{star}} [M_{\odot}]) = 8.5-11.5$, aimed at characterizing their overall statistical behavior in given mass range. The results are presented and discussed in Section 4 & 5. We also quantitatively assess the statistical relevance of all scaling relation shown in the Table 1. The key conclusions of this work are as follows:

- In Figure 6, we show that the low-mass galaxies ($M_{\text{star}} < 10^{9.5} M_{\odot}$) are DM dominated with average $\langle f_{\text{DM}} \rangle \approx 0.85$ within both the R_{e} (inner regions) and R_{out} (outskirts). This suggests that strong stellar feedback and other environmental effects (e.g., ram pressure stripping, tidal interactions) mostlikely remove the gas from galaxies, which makes the star-formation inefficient maintaining low baryon-surface density, i.e., shallow baryonic potential, and hence DM dominates across the galactic radius.
- In high-mass ($M_{\text{star}} \geq 10^{10} M_{\odot}$) galaxies the DM fraction is low within the inner regions compared to their outskirts. At fixed circular velocity low-mass galaxies ($M_{\text{star}} < 10^{9.5} M_{\odot}$) exhibit about $\sim 40\%$ higher DM fraction than their high-mass counterparts within R_{e} . On the other hand, outskirts of both high- and low-mass systems show no significant change (less than 10%) in DM fractions. This suggests an inside-out disk growth. These findings are consistent with the predictions of local spirals and previous high- z disk-like galaxies.

- We report that the DM fraction inversely correlates with baryon surface density within the inner regions and outskirts (see Figure 8), resembling correlations established in local star-forming disk galaxies. The relation we obtain is very tight with an intrinsic scatter of $0.11 - 0.13$ dex. The existence of such a correlation is consistent with the *inside-out baryon assembly scenario* in which the central component of star-forming galaxies form first, from gas that have lower specific angular momentum, dense, and has potentially undergone compaction. In contrast, the outer part of star-forming galaxies form later, from gas that is accreted at later epochs and brings higher specific angular momentum.
- Within the redshift range of the MAGPI sample ($z = 0.1 - 0.85$), we observe no significant evolution in $f_{\text{DM}}(z)$ (see Figures 9 & 10). When combined with the GS25 high-redshift dataset, we find the magnitude of evolution between $z = 0.1 - 2.0$ depends on stellar mass with low mass galaxies, ($M_{\text{star}} \leq 10^{9.5} M_{\odot}$) showing the strongest evolution. At high mass, $M_{\text{star}} > 10^{10} M_{\odot}$ our results are consistent with Nestor Shachar et al. 2023 but are not statistically significant. At $z > 0.75$ the sample is dominated by high mass galaxies ($M_{\text{star}} > 10^{9.5} M_{\odot}$), while the MAGPI sample is dominated by low mass galaxies ($M_{\text{star}} \leq 10^{9.5} M_{\odot}$) making the need for samples with large dynamic ranges increasingly clear.
- The observed invariance of f_{DM} with redshift, together with its strong dependence on Σ_{bar} and M_{star} , agree with hydrodynamical simulations (like IllustrisTNG and EAGLE) which emphasize the importance of feedback-regulated growth and halo response in preserving an almost fixed baryon-to-dark-matter ratio within both R_{e} and R_{opt} .

Together, these results provide strong empirical support for a scenario in which disk galaxies assemble their baryons and DM in a coordinated fashion, with the dominant mass component depending on galaxy mass, scale, and baryonic concentration—but not significantly on redshift within $z \approx 0.1 - 1.5$. Next generation high-resolution IFU surveys at $z > 1$ targeting lower-mass systems will be critical for disentangling observational biases and further constraining the co-evolution of baryons and DM in galaxies.

Acknowledgments

GS acknowledge funding from the European Union’s Horizon 2020 research and innovation programme under the Marie Skłodowska-Curie Grant agreement ID No.: 101147719. Although project is funded by the European Union, views and opinions expressed in this work are however those of the author(s) only and do not necessarily reflect those of the European Union. Neither the European Union nor the granting authority can be held responsible for them. G.S. acknowledges support from the SARAO Postdoctoral Fellowship (UID 97882), under which the MAGPI project, Dark Matter Halos of Intermediate-Redshift Galaxies, was initiated. GS acknowledge the use of the ilifu cloud computing facility – www.ilifu.ac.za, a partnership between the University of Cape Town, the University of the Western Cape, Stellenbosch University, Sol Plaatje University and the Cape Peninsula University of Technology. The ilifu facility is supported by contributions from the Inter-University Institute for Data Intensive Astronomy (IDIA – a partnership between the University of Cape Town, the University of Pretoria and the University of the Western Cape), the Computational Biology division at UCT and the Data Intensive Research Initiative of South Africa (DIRISA).

GS also acknowledge the funding from IRMIA++ fellowship where this project has been continued. GS thanks Benoit Famaey, Mihael Petac, and Jonathan Freundlich for various discussions. A part of this research was supported by funding from the University of Strasbourg Institute for Advanced Study (USIAS) within the French national programme “Investment for the Future” (Excellence Initiative) IdEx-Unistra, under the leadership of Florent Renaud. CL, TM and CF are the recipient of the Australian Research Council Discovery Project DP210101945. Based on observations collected at the European Organisation for Astronomical Research in the Southern Hemisphere under ESO program 1104.B-0536. We wish to thank the ESO staff, and in particular the staff at Paranal Observatory, for carrying out the MAGPI observations. MAGPI targets were selected from GAMA. GAMA is a joint European-Australasian project based around a spectroscopic campaign using the Anglo-Australian Telescope. GAMA is funded by the STFC (UK), the ARC (Australia), the AAO, and the participating institutions. GAMA photometry is based on observations made with ESO Telescopes at the La Silla Paranal Observatory under programme ID 179.A-2004, ID 177.A-3016. CF is the recipient of an Australian Research Council Future Fellowship (project number FT210100168) funded by the Australian Government. SMS acknowledges funding from the Australian Research Council (DE220100003). Parts of this research were conducted by the Australian Research Council Centre of Excellence for All Sky Astrophysics in 3 Dimensions (ASTRO 3D), through project number CE170100013. I.B. has received funding from the European Union’s Horizon 2020 research and innovation programme under the Marie Skłodowska-Curie Grant agreement ID n.o 101059532. This project was extended for 6 months by the Franziska Seidl Funding Program of the University of Vienna. LMV acknowledges support by the German Academic Scholarship Foundation (Studienstiftung des deutschen Volkes) and the Marianne-Plehn-Program of the Elite Network of Bavaria. KH acknowledges support by the Royal Society through a Dorothy Hodgkin Fellowship to KA Oman (DHF/R1/231105) S.K.Y. acknowledges support from the Korean National Research Foundation (RS-2025-00514475; RS-2022-NR070872).

A Pressure support correction

Before disentangling the baryonic components and estimating the DM fraction from RCs, we applied the correction for pressure support on observed RCs, following the pressure gradient correction (PGC) method, introduced in [48, Sec. 3.2], defined as:

$$V_c^{PGC} = \sqrt{V_\phi^2 - \sigma_R^2 \left[\frac{\partial \ln \Sigma}{\partial \ln R} + \frac{\partial \ln \sigma_R^2}{\partial \ln R} + \frac{1}{2}(1 - \alpha) \right]} \quad (\text{A.1})$$

where V_c^{PGC} is the pressure gradient corrected circular velocity, V_ϕ is the inclination-corrected rotation velocity, Σ is 2D-density e.g., H_α , mass surface density, and σ_R is radial velocity dispersion. Here, we follow [127] in which velocity anisotropy $(1 - \sigma_\phi^2/\sigma_R^2)$ is given as $(1 - \alpha)/2$, where α is the radial slope of the rotation velocity ($\alpha = \partial \ln V_\phi / \partial \ln R$). From the kinematic modelling of the datacubes (discussed in Section 2.2), we have required information about Σ , σ_R and V_ϕ to employ into the Equation A.1. Let us remark, all the quantities (namely: V_ϕ , σ_R , and Σ) are function of radius (R)⁶, and they are derived from datacubes.

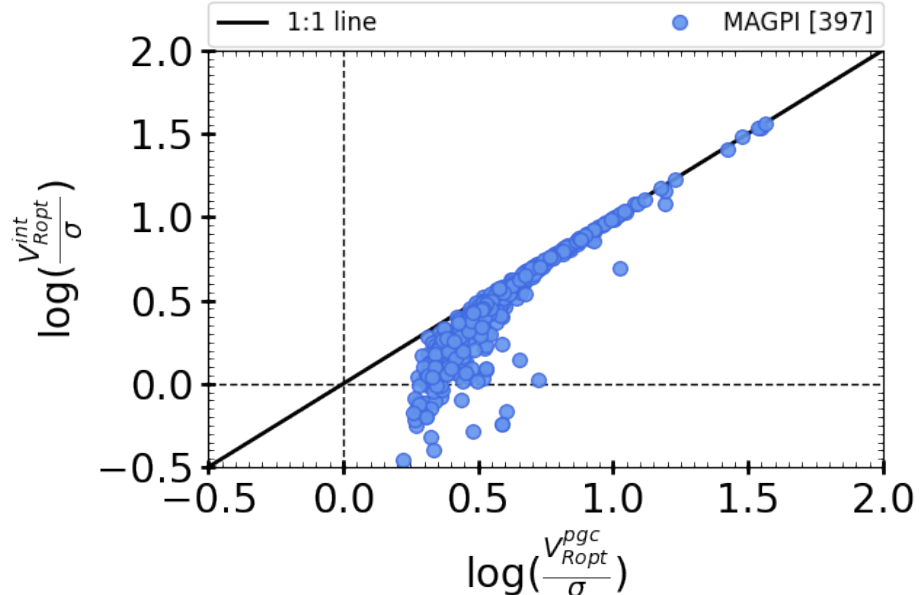


Figure 13. Comparison of the intrinsic and pressure-corrected rotation-to-dispersion ratios for the MAGPI galaxy sample. The x -axis shows $V_{R\text{out}}^{\text{PGC}}/\sigma$, the pressure-corrected rotation velocity ratio, while the y -axis shows the intrinsic (uncorrected) $V_{R\text{out}}^{\text{int}}/\sigma$. Each point represents a galaxy; the solid black line indicates the 1:1 relation. The plot highlights how galaxies initially appearing dispersion-dominated shift toward rotation-supported regimes after applying the pressure gradient correction.

Equation A.1 correct for the impact of turbulent gas velocity dispersion in high- z galaxies, which can lower the observed rotation velocity, particularly in the inner regions and in many cases also in the outskirts. In this work, we applied PGC to full dataset used in our work, this ensures that gas pressure dominated (or turbulent velocity dispersion) systems are

⁶i.e., $V_\phi = V_\phi(R)$, $\sigma_R = \sigma_R(R)$, $\Sigma = \Sigma(R)$, and $\alpha = \alpha(R)$

properly corrected and can be included in the analysis without bias. For details of the PGC procedure and its impact on the rotation curves, we refer the reader to [48, Appendix C].

In Figure 13, we demonstrate the effect of the pressure gradient on the kinematics of galaxies in our MAGPI sample. We compare the intrinsic rotation-to-dispersion ratio ($V_{\text{Ropt}}^{\text{int}}/\sigma$), uncorrected for pressure support, to the pressure-corrected ratio ($V_{\text{Ropt}}^{\text{PGC}}/\sigma$). The data points show that many galaxies initially classified as dispersion-dominated (with low $V_{\text{Ropt}}^{\text{int}}/\sigma$) move closer to or above the 1:1 line after applying PGC, indicating that their true kinematics are rotation-supported. This confirms that the PGC method effectively accounts for the impact of turbulent pressure on rotation velocity, allowing inclusion of these galaxies in our analysis.

B Gas masses

Observations show that typical star-forming galaxies lie on a relatively tight, almost linear, redshift-dependent relation between their stellar mass and star formation rate, the so-called main sequence of star formation [e.g., 83, 128, 129]. Most stars since $z \sim 2.5$ were formed on and around this MS [e.g., 130], and galaxies that constitute it, usually exhibit a rotating disk morphology [e.g., 90, 131, 132]. Figure 1 shows the position of the final sample (detailed in Section 2.3) with respect to the main sequence of typical star-forming galaxies (MS), i.e., their offset from the main sequence:

$$\delta\text{MS} = \text{SFR}/\text{SFR}(\text{MS}; z, M_{\text{star}}), \quad (\text{B.1})$$

where $\text{SFR}(\text{MS}; z, M_{\text{star}})$ is the analytical prescription for the center of the MS as a function of redshift and stellar mass proposed in the compilation by [83]. This figure shows that majority of the galaxies in the total sample are within the $2 - 3\sigma$ range of SFMS. This enables us to estimate their molecular gas masses (M_{H_2}) using the [89] scaling relations, which provide a parameterization of the molecular gas mass (including the Helium content) as a function of redshift, stellar mass, and offset from the MS stemming from a large sample of about 1400 sources on and around the MS in the range $z = 0 - 4.5$ (see also [133] and [134]). The scatter around these molecular gas scaling relations and the stellar mass induces a 0.3 dex uncertainty in the molecular gas mass estimates, which is accounted in the f_{DM} error estimates. The H₂ mass of our sample is $7.75 \leq \log(M_{\text{H}_2} [M_{\odot}]) \leq 10.18$, with an average molecular gas fractions ($f_{\text{H}_2} = \frac{M_{\text{H}_2}}{M_{\text{bar}}}$) of 0.10 ± 0.06 .

To calculate the atomic mass (M_{HI}) content of galaxies within the redshift range $0.1 \leq z \leq 0.85$, we use the HI scaling relation presented by [135] at $z = 0.2 - 0.5$, and [106] at $z > 0.5$. The relation was derived using a stacking analysis across three stellar mass bins, each bin with a 4σ detection and an average uncertainty of ~ 0.3 dex. This uncertainty in the gas scaling relation is additionally accounted in the error of HI mass estimates and propagated with MCMC when estimating the f_{DM} . The HI Mass range of our sample is $8.62 \leq \log(M_{\text{HI}} [M_{\odot}]) \leq 10.68$, with an average atomic gas fractions ($f_{\text{HI}} = \frac{M_{\text{HI}}}{M_{\text{bar}}}$) of 0.57 ± 0.19 . for further details of gas mass computation, we refer reader to [52].

C Full-spectral fitting stellar masses

In the main analysis, stellar masses were estimated via broad-band photometric spectral energy distribution (SED) fitting, following the methodology outlined in [82]. While this technique yields reliable global mass estimates, we observe that a very small subset (n=3)

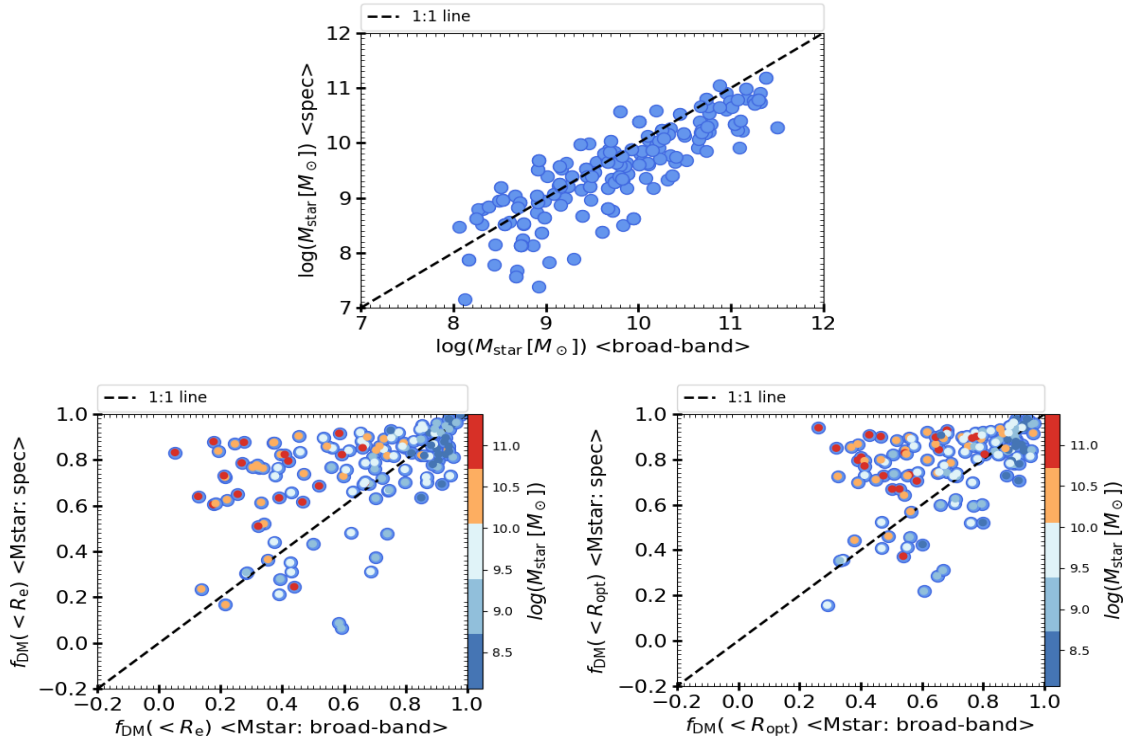


Figure 14. Impact of stellar mass estimation techniques on DM Fraction measurements. *Top panel:* Comparison between stellar masses derived from SED fitting using broad band images (used in this study; Bellstedt et al.) and those estimated using spatially resolved spectra-fitting techniques by Poci et al. (in preparation). *Bottom panel:* Comparison of DM fractions within R_e (left) and R_{opt} (right). The x-axis shows f_{DM} computed using Bellstedt et al. stellar masses (broad-band), while the y-axis shows values based on Poci et al. estimates (spec). Data points are color-coded by the SED-derived stellar mass. The black dashed in all panels shows the one-to-one line for reference.

of massive ($M_{\text{star}} > 10^{10} M_{\odot}$) galaxies in our sample exhibit unphysical (i.e., negative) DM fractions. Therefore, to assess the robustness of our DM fraction (f_{DM}) measurements, we compare them to estimates based on stellar masses derived using a full-spectral fitting technique (Poci et al., in preparation).

In this method, each MAGPI mini-cube is spatially-integrated to produce a single spectrum. For the subset of galaxies for which this spectrum has $S/N > 20$, we fit them in pPXF [136] using the E-MILES SSP library [137] assuming a Chabrier IMF. From the resulting star-formation history, we compute the stellar mass-to-light ratio, and from the spectrum itself we compute the spatially-integrated luminosity over the same spectral window. This results in a spatially-integrated stellar mass.

Figure 14, presents the resulting f_{DM} values computed using these full-spectral stellar masses. We find that broad-band SED fitting based stellar masses are systematically higher than those derived via full-spectral fitting. Consequently, especially in high-mass systems, the DM fractions derived in this work maybe underestimated by more than 50%—leading to the appearance of “dark matter-deficient ($f_{\text{DM}} < 20\%$)” galaxies. In the low mass galaxies this difference is only within $\pm 5 - 10\%$. That is, applying full spectral-fitting based stellar

masses significantly increases the inferred f_{DM} within both R_e and R_{opt} , reaffirming that even the most massive galaxies in our sample contain substantial DM components. Nevertheless, as the full-spectral fitting stellar masses are not yet available for full sample, we adopt the photometric SED-based stellar masses as our baseline for all primary analyses presented in this study.

References

- [1] P.J.E. Peebles, *Principles of Physical Cosmology*, Princeton university press (1993), [10.1515/9780691206721](https://doi.org/10.1515/9780691206721).
- [2] V.C. Rubin, W.K. Ford Jr and N. Thonnard, *Rotational properties of 21 sc galaxies with a large range of luminosities and radii, from ngc 4605/r= 4kpc/to ugc 2885/r= 122 kpc*, *The Astrophysical Journal* **238** (1980) 471.
- [3] A. Bosma, *21-cm line studies of spiral galaxies. i-observations of the galaxies ngc 5033, 3198, 5055, 2841, and 7331*, *The Astronomical Journal* **86** (1981) 1791.
- [4] Y. Sofue and V. Rubin, *Rotation Curves of Spiral Galaxies*, *ARA&A* **39** (2001) 137 [[astro-ph/0010594](https://arxiv.org/abs/astro-ph/0010594)].
- [5] P. Salucci, *The distribution of dark matter in galaxies*, *A&AR* **27** (2019) 2 [[1811.08843](https://arxiv.org/abs/1811.08843)].
- [6] R.E. Angulo and O. Hahn, *Large-scale dark matter simulations*, *Living Reviews in Computational Astrophysics* **8** (2022) 1 [[2112.05165](https://arxiv.org/abs/2112.05165)].
- [7] J.S. Bullock and M. Boylan-Kolchin, *Small-Scale Challenges to the Λ CDM Paradigm*, *ARA&A* **55** (2017) 343 [[1707.04256](https://arxiv.org/abs/1707.04256)].
- [8] L.V. Sales, A. Wetzel and A. Fattahi, *Baryonic solutions and challenges for cosmological models of dwarf galaxies*, *Nature Astronomy* **6** (2022) 897 [[2206.05295](https://arxiv.org/abs/2206.05295)].
- [9] M. Boylan-Kolchin, J.S. Bullock and M. Kaplinghat, *Too big to fail? The puzzling darkness of massive Milky Way subhaloes*, *MNRAS* **415** (2011) L40 [[1103.0007](https://arxiv.org/abs/1103.0007)].
- [10] K.A. Oman, J.F. Navarro, A. Fattahi, C.S. Frenk, T. Sawala, S.D.M. White et al., *The unexpected diversity of dwarf galaxy rotation curves*, *MNRAS* **452** (2015) 3650 [[1504.01437](https://arxiv.org/abs/1504.01437)].
- [11] S.A. Kassin, R.S. de Jong and B.J. Weiner, *Dark and Baryonic Matter in Bright Spiral Galaxies. II. Radial Distributions for 34 Galaxies*, *ApJ* **643** (2006) 804 [[astro-ph/0602027](https://arxiv.org/abs/astro-ph/0602027)].
- [12] T.P.K. Martinsson, M.A.W. Verheijen, K.B. Westfall, M.A. Bershady, D.R. Andersen and R.A. Swaters, *The DiskMass Survey. VII. The distribution of luminous and dark matter in spiral galaxies*, *A&A* **557** (2013) A131 [[1308.0336](https://arxiv.org/abs/1308.0336)].
- [13] S. Courteau and A.A. Dutton, *On the Global Mass Distribution in Disk Galaxies*, *ApJL* **801** (2015) L20 [[1502.04709](https://arxiv.org/abs/1502.04709)].
- [14] M. Cappellari, N. Scott, K. Alatalo, L. Blitz, M. Bois, F. Bournaud et al., *The ATLAS^{3D} project - XV. Benchmark for early-type galaxies scaling relations from 260 dynamical models: mass-to-light ratio, dark matter, Fundamental Plane and Mass Plane*, *MNRAS* **432** (2013) 1709 [[1208.3522](https://arxiv.org/abs/1208.3522)].
- [15] W.E. Harris, R.-S. Remus, G.L.H. Harris and I.V. Babyk, *Measuring Dark Matter in Galaxies: The Mass Fraction within Five Effective Radii*, *ApJ* **905** (2020) 28 [[2010.14372](https://arxiv.org/abs/2010.14372)].
- [16] D. Thomas, C. Maraston, R. Bender and C. Mendes de Oliveira, *The Epochs of Early-Type Galaxy Formation as a Function of Environment*, *ApJ* **621** (2005) 673 [[astro-ph/0410209](https://arxiv.org/abs/astro-ph/0410209)].
- [17] D. Thomas, C. Maraston, K. Schawinski, M. Sarzi and J. Silk, *Environment and self-regulation in galaxy formation*, *MNRAS* **404** (2010) 1775 [[0912.0259](https://arxiv.org/abs/0912.0259)].

[18] P. Catelan and T. Theuns, *Evolution of the angular momentum of protogalaxies from tidal torques: Zel'dovich approximation*, *MNRAS* **282** (1996) 436 [[astro-ph/9604077](#)].

[19] K. El-Badry, E. Quataert, A. Wetzel, P.F. Hopkins, D.R. Weisz, T.K. Chan et al., *Gas kinematics, morphology and angular momentum in the FIRE simulations*, *MNRAS* **473** (2018) 1930 [[1705.10321](#)].

[20] S. Garrison-Kimmel, P.F. Hopkins, A. Wetzel, K. El-Badry, R.E. Sanderson, J.S. Bullock et al., *The origin of the diverse morphologies and kinematics of Milky Way-mass galaxies in the FIRE-2 simulations*, *MNRAS* (2018) [[1712.03966](#)].

[21] C.D.P. Lagos, *Angular Momentum Evolution of Galaxies: the Perspective of Hydrodynamical Simulations*, in *IAU General Assembly*, pp. 208–214, Mar., 2020, [DOI](#).

[22] A. Dekel and A. Burkert, *Wet disc contraction to galactic blue nuggets and quenching to red nuggets*, *MNRAS* **438** (2014) 1870 [[1310.1074](#)].

[23] A. Zolotov, A. Dekel, N. Mandelker, D. Tweed, S. Inoue, C. DeGraf et al., *Compaction and quenching of high- z galaxies in cosmological simulations: blue and red nuggets*, *MNRAS* **450** (2015) 2327 [[1412.4783](#)].

[24] M. Danovich, A. Dekel, O. Hahn, D. Ceverino and J. Primack, *Four phases of angular-momentum buildup in high- z galaxies: from cosmic-web streams through an extended ring to disc and bulge*, *MNRAS* **449** (2015) 2087 [[1407.7129](#)].

[25] S. Waterval, C. Cannarozzo and A.V. Macciò, *Gas accretion at high redshift: cold flows all the way*, *MNRAS* **537** (2025) 2726 [[2501.19009](#)].

[26] A. Pontzen and F. Governato, *How supernova feedback turns dark matter cusps into cores*, *MNRAS* **421** (2012) 3464 [[1106.0499](#)].

[27] A. Pontzen and F. Governato, *Cold dark matter heats up*, *Nature* **506** (2014) 171 [[1402.1764](#)].

[28] A.A. Dutton, A.V. Macciò, A. Dekel, L. Wang, G. Stinson, A. Obreja et al., *NIHAO IX: the role of gas inflows and outflows in driving the contraction and expansion of cold dark matter haloes*, *MNRAS* **461** (2016) 2658 [[1605.05323](#)].

[29] A.A. El-Zant, J. Freundlich and F. Combes, *From cusps to cores: a stochastic model*, *MNRAS* **461** (2016) 1745 [[1603.00526](#)].

[30] J. Freundlich, A. Dekel, F. Jiang, G. Ishai, N. Cornuault, S. Lapiner et al., *A model for core formation in dark matter haloes and ultra-diffuse galaxies by outflow episodes*, *MNRAS* **491** (2020) 4523 [[1907.11726](#)].

[31] A. Dekel, J. Freundlich, F. Jiang, S. Lapiner, A. Burkert, D. Ceverino et al., *Core formation in high- z massive haloes: heating by post-compaction satellites and response to AGN outflows*, *MNRAS* **508** (2021) 999 [[2106.01378](#)].

[32] Z. Li, A. Dekel, N. Mandelker, J. Freundlich and T.L. François, *The response of dark matter haloes to gas ejection: CuspCore II*, *MNRAS* **518** (2023) 5356 [[2206.07069](#)].

[33] N.M. Förster Schreiber and S. Wuyts, *Star-forming galaxies at cosmic noon*, *Annual Review of Astronomy and Astrophysics* **58** (2020) null [<https://doi.org/10.1146/annurev-astro-032620-021910>].

[34] S. Fujimoto, A.L. Faisst, A. Tsujita, M. Kohandel, L.L. Lee, H. Übler et al., *The ALPINE-CRISTAL-JWST Survey: NIRSpec IFU Data Processing and Spatially-resolved Views of Chemical Enrichment in Normal Galaxies at $z=4$ -6*, *arXiv e-prints* (2025) [arXiv:2510.16116](#) [[2510.16116](#)].

[35] H. Übler, F. D'Eugenio, M. Perna, S. Arribas, G.C. Jones, A.J. Bunker et al., *GA-NIFS: NIRSpec reveals evidence for non-circular motions and AGN feedback in GN20*, *MNRAS* **533** (2024) 4287 [[2403.03192](#)].

[36] R. Genzel, N.F. Schreiber, H. Ubler, P. Lang, T. Naab, R. Bender et al., *Strongly baryon-dominated disk galaxies at the peak of galaxy formation ten billion years ago*, *Nature* **543** (2017) 397.

[37] P. Lang, N.M.F. Schreiber, R. Genzel, S. Wuyts, E. Wisnioski, A. Beifiori et al., *Falling outer rotation curves of star-forming galaxies at $0.6 \lesssim z \lesssim 2.6$ probed with KMOS3d and SINS/zC-SINF*, *The Astrophysical Journal* **840** (2017) 92.

[38] M. Persic, P. Salucci and F. Stel, *The universal rotation curve of spiral galaxies—i. the dark matter connection*, *Monthly Notices of the Royal Astronomical Society* **281** (1996) 27.

[39] A. Burkert, N.F. Schreiber, R. Genzel, P. Lang, L. Tacconi, E. Wisnioski et al., *The angular momentum distribution and baryon content of star-forming galaxies at $z = 1-3$* , *The Astrophysical Journal* **826** (2016) 214.

[40] S. Wuyts, N.M. Förster Schreiber, E. Wisnioski, R. Genzel, A. Burkert, K. Bandara et al., *KMOS3D: Dynamical Constraints on the Mass Budget in Early Star-forming Disks*, *ApJ* **831** (2016) 149 [[1603.03432](#)].

[41] S.H. Price, M. Kriek, A.E. Shapley, N.A. Reddy, W.R. Freeman, A.L. Coil et al., *The MOSDEF Survey: Dynamical and Baryonic Masses and Kinematic Structures of Star-forming Galaxies at $1.4 \leq z \leq 2.6$* , *ApJ* **819** (2016) 80 [[1511.03272](#)].

[42] H. Übler, R. Genzel, L.J. Tacconi, N.M.F. Schreiber, R. Neri, A. Contursi et al., *Ionized and molecular gas kinematics in a $z = 1.4$ star-forming galaxy*, *The Astrophysical Journal* **854** (2018) L24.

[43] R. Genzel, S.H. Price, H. Übler, N.M. Förster Schreiber, T.T. Shimizu, L.J. Tacconi et al., *Rotation Curves in $z \sim 1-2$ Star-forming Disks: Evidence for Cored Dark Matter Distributions*, *ApJ* **902** (2020) 98 [[2006.03046](#)].

[44] J.T. Mendel, A. Beifiori, R.P. Saglia, R. Bender, G.B. Brammer, J. Chan et al., *The Kinematics of Massive Quiescent Galaxies at $1.4 \leq z \leq 2.1$: Dark Matter Fractions, IMF Variation, and the Relation to Local Early-type Galaxies*, *ApJ* **899** (2020) 87 [[2006.13949](#)].

[45] S.H. Price, T.T. Shimizu, R. Genzel, H. Übler, N.M. Förster Schreiber, L.J. Tacconi et al., *Rotation Curves in $z = 1-2$ Star-forming Disks: Comparison of Dark Matter Fractions and Disk Properties for Different Fitting Methods*, *ApJ* **922** (2021) 143 [[2109.02659](#)].

[46] A. Nestor Shachar, S.H. Price, N.M. Förster Schreiber, R. Genzel, T.T. Shimizu, L.J. Tacconi et al., *RC100: Rotation Curves of 100 Massive Star-forming Galaxies at $z = 0.6-2.5$ Reveal Little Dark Matter on Galactic Scales*, *ApJ* **944** (2023) 78 [[2209.12199](#)].

[47] A.L. Tiley, A. Swinbank, C. Harrison, I. Smail, O. Turner, M. Schaller et al., *The shapes of the rotation curves of star-forming galaxies over the last ≈ 10 gyr*, *Monthly Notices of the Royal Astronomical Society* **485** (2019) 934.

[48] G. Sharma, P. Salucci, C.M. Harrison, G. van de Ven and A. Lapi, *Flat rotation curves of $z \sim 1$ star-forming galaxies*, *MNRAS* **503** (2021) 1753 [[2005.00279](#)].

[49] R. Sharples, *KMOS @ the VLT: Commissioning and Early Science*, in *Galaxies in 3D across the Universe*, B.L. Ziegler, F. Combes, H. Dannerbauer and M. Verdugo, eds., vol. 309 of *IAU Symposium*, pp. 11–16, Feb., 2015, [DOI](#).

[50] J.P. Stott, A. Swinbank, H.L. Johnson, A. Tiley, G. Magdis, R. Bower et al., *The kmos redshift one spectroscopic survey (kross): dynamical properties, gas and dark matter fractions of typical $z \sim 1$ star-forming galaxies*, *Monthly Notices of the Royal Astronomical Society* **457** (2016) 1888.

[51] G. Sharma, P. Salucci and G. van de Ven, *Dark matter fraction in $z \sim 1$ star-forming galaxies*, *A&A* **653** (2021) A20 [[2105.13684](#)].

[52] G. Sharma, G. van de Ven, P. Salucci and M. Martorano, *Dark matter fraction in disk-like galaxies over the past 10 Gyr*, *A&A* **699** (2025) A164 [[2309.04541](#)].

[53] B.I. Ciocan, N.F. Bouché, J. Fensch, W. Mercier, D. Krajnović, J. Richard et al., *MUSE-DARK-I: Dark matter halo properties of intermediate- z star-forming galaxies*, *arXiv e-prints* (2025) arXiv:2506.19721 [[2506.19721](#)].

[54] N.F. Bouché, S. Bera, D. Krajnović, E. Emsellem, W. Mercier, J. Schaye et al., *The MUSE Extremely Deep Field: Evidence for SFR-induced cores in dark-matter dominated galaxies at $z \simeq 1$* , *A&A* **658** (2022) A76 [[2109.07545](#)].

[55] C. Foster, J.T. Mendel, C.D.P. Lagos, E. Wisnioski, T. Yuan, F. D'Eugenio et al., *The MAGPI survey: Science goals, design, observing strategy, early results and theoretical framework*, *PASA* **38** (2021) e031 [[2011.13567](#)].

[56] S.P. Driver, D.T. Hill, L.S. Kelvin, A.S.G. Robotham, J. Liske, P. Norberg et al., *Galaxy and Mass Assembly (GAMA): survey diagnostics and core data release*, *MNRAS* **413** (2011) 971 [[1009.0614](#)].

[57] S.P. Driver, S. Bellstedt, A.S.G. Robotham, I.K. Baldry, L.J. Davies, J. Liske et al., *Galaxy And Mass Assembly (GAMA): Data Release 4 and the $z \gtrsim 0.1$ total and $z \gtrsim 0.08$ morphological galaxy stellar mass functions*, *MNRAS* **513** (2022) 439 [[2203.08539](#)].

[58] J. Richard, J.P. Kneib, M. Limousin, A. Edge and E. Jullo, *Abell 370 revisited: refurbished Hubble imaging of the first strong lensing cluster*, *MNRAS* **402** (2010) L44 [[0910.5553](#)].

[59] D.J. Lagattuta, J. Richard, B. Clément, G. Mahler, V. Patrício, R. Pelló et al., *Lens modelling Abell 370: crowning the final frontier field with MUSE*, *MNRAS* **469** (2017) 3946 [[1611.01513](#)].

[60] H. Ebeling, A.C. Edge, A. Mantz, E. Barrett, J.P. Henry, C.J. Ma et al., *The X-ray brightest clusters of galaxies from the Massive Cluster Survey*, *MNRAS* **407** (2010) 83 [[1004.4683](#)].

[61] G. Mahler, J. Richard, B. Clément, D. Lagattuta, K. Schmidt, V. Patrício et al., *Strong-lensing analysis of A2744 with MUSE and Hubble Frontier Fields images*, *MNRAS* **473** (2018) 663 [[1702.06962](#)].

[62] J. Hartke, D. Kakkad, C. Reyes, C. Moya-Sierralta, A. Reyes, T. Kravtsov et al., *MUSE+GALACSI: the first years*, in *Adaptive Optics Systems VII*, L. Schreiber, D. Schmidt and E. Vernet, eds., vol. 11448 of *Society of Photo-Optical Instrumentation Engineers (SPIE) Conference Series*, p. 114480V, Dec., 2020, DOI.

[63] P.M. Weilbacher, R. Palsa, O. Streicher, R. Bacon, T. Urrutia, L. Wisotzki et al., *The data processing pipeline for the MUSE instrument*, *A&A* **641** (2020) A28 [[2006.08638](#)].

[64] K.T. Soto, S.J. Lilly, R. Bacon, J. Richard and S. Conseil, *ZAP - enhanced PCA sky subtraction for integral field spectroscopy*, *MNRAS* **458** (2016) 3210 [[1602.08037](#)].

[65] A.S.G. Robotham, L.J.M. Davies, S.P. Driver, S. Koushan, D.S. Tararu, S. Casura et al., *ProFound: Source Extraction and Application to Modern Survey Data*, *MNRAS* **476** (2018) 3137 [[1802.00937](#)].

[66] A. Bittner, J. Falcón-Barroso, B. Nedelchev, A. Dorta, D.A. Gadotti, M. Sarzi et al., *The GIST pipeline: A multi-purpose tool for the analysis and visualisation of (integral-field) spectroscopic data*, *A&A* **628** (2019) A117 [[1906.04746](#)].

[67] A.S.G. Robotham, D.S. Tararu, R. Tobar, A. Moffett and S.P. Driver, *PROFIT: Bayesian profile fitting of galaxy images*, *MNRAS* **466** (2017) 1513 [[1611.08586](#)].

[68] R.B. Tully and J.R. Fisher, *A new method of determining distances to galaxies.*, *A&A* **54** (1977) 661.

[69] A.-M. Weijmans, P.T. de Zeeuw, E. Emsellem, D. Krajnović, P.-Y. Lablanche, K. Alatalo et al., *The ATLAS^{3D} project - XXIV. The intrinsic shape distribution of early-type galaxies*, *MNRAS* **444** (2014) 3340 [[1408.1099](#)].

[70] C. Harrison, H. Johnson, A. Swinbank, J. Stott, R. Bower, I. Smail et al., *The kmos redshift one spectroscopic survey (kross): rotational velocities and angular momentum of $z \approx 0.9$ galaxies*, *Monthly Notices of the Royal Astronomical Society* **467** (2017) 1965.

[71] N.D. Padilla and M.A. Strauss, *The shapes of galaxies in the Sloan Digital Sky Survey*, *MNRAS* **388** (2008) 1321 [[0802.0877](#)].

[72] C.T. Unterborn and B.S. Ryden, *Inclination-Dependent Extinction Effects in Disk Galaxies in the Sloan Digital Sky Survey*, *ApJ* **687** (2008) 976 [[0801.2400](#)].

[73] S. Rodríguez and N.D. Padilla, *The intrinsic shape of galaxies in SDSS/Galaxy Zoo*, *MNRAS* **434** (2013) 2153 [[1306.3264](#)].

[74] S.R. Hinton, T.M. Davis, C. Lidman, K. Glazebrook and G.F. Lewis, *MARZ: Manual and automatic redshifting software*, *Astronomy and Computing* **15** (2016) 61 [[1603.09438](#)].

[75] D.E. Osterbrock and G.J. Ferland, *Astrophysics of gaseous nebulae and active galactic nuclei*, University science books (2006).

[76] E.L. Fitzpatrick, D. Massa, K.D. Gordon, R. Bohlin and G.C. Clayton, *An Analysis of the Shapes of Interstellar Extinction Curves. VII. Milky Way Spectrophotometric Optical-through-ultraviolet Extinction and Its R-dependence*, *ApJ* **886** (2019) 108 [[1910.08852](#)].

[77] D. Calzetti, *Star Formation Rate Indicators*, in *Secular Evolution of Galaxies*, J. Falcón-Barroso and J.H. Knapen, eds., p. 419 (2013), [DOI](#).

[78] P. Kroupa, C. Weidner, J. Pflamm-Altenburg, I. Thies, J. Dabringhausen, M. Marks et al., *The Stellar and Sub-Stellar Initial Mass Function of Simple and Composite Populations*, in *Planets, Stars and Stellar Systems. Volume 5: Galactic Structure and Stellar Populations*, T.D. Oswalt and G. Gilmore, eds., vol. 5, p. 115 (2013), [DOI](#).

[79] G. Bruzual and S. Charlot, *Stellar population synthesis at the resolution of 2003*, *MNRAS* **344** (2003) 1000 [[astro-ph/0309134](#)].

[80] S. Charlot and S.M. Fall, *A Simple Model for the Absorption of Starlight by Dust in Galaxies*, *ApJ* **539** (2000) 718 [[astro-ph/0003128](#)].

[81] J.E. Dale, J. Ngoumou, B. Ercolano and I.A. Bonnell, *Before the first supernova: combined effects of H II regions and winds on molecular clouds*, *MNRAS* **442** (2014) 694 [[1404.6102](#)].

[82] S. Bellstedt, A.S.G. Robotham, S.P. Driver, J.E. Thorne, L.J.M. Davies, C.d.P. Lagos et al., *Galaxy And Mass Assembly (GAMA): a forensic SED reconstruction of the cosmic star formation history and metallicity evolution by galaxy type*, *MNRAS* **498** (2020) 5581 [[2005.11917](#)].

[83] J.S. Speagle, C.L. Steinhardt, P.L. Capak and J.D. Silverman, *A highly consistent framework for the evolution of the star-forming “main sequence” from $z = 0$ -6*, *The Astrophysical Journal Supplement Series* **214** (2014) 15.

[84] E.D. Teodoro and F. Fraternali, *3d barolo: a new 3d algorithm to derive rotation curves of galaxies*, *Monthly Notices of the Royal Astronomical Society* **451** (2015) 3021.

[85] E. Di Teodoro, F. Fraternali and S. Miller, *Flat rotation curves and low velocity dispersions in kmos star-forming galaxies at $z = 1$* , *Astronomy & Astrophysics* **594** (2016) A77.

[86] E. Wisnioski, N.M. Förster Schreiber, S. Wuyts, E. Wuyts, K. Bandara, D. Wilman et al., *The KMOS^{3D} Survey: Design, First Results, and the Evolution of Galaxy Kinematics from $0.7 \leq z \leq 2.7$* , *ApJ* **799** (2015) 209 [[1409.6791](#)].

[87] R.O. Amorín, M. Rodríguez-Henríquez, V. Fernández, J.M. Vílchez, R. Marques-Chaves, D. Schaefer et al., *Ubiquitous broad-line emission and the relation between ionized gas outflows and Lyman continuum escape in Green Pea galaxies*, *A&A* **682** (2024) L25 [[2401.04278](#)].

[88] A. Zurita, M. Relaño, J.E. Beckman and J.H. Knapen, *Ionized gas kinematics and massive star formation in NGC 1530*, *A&A* **413** (2004) 73 [[astro-ph/0307234](#)].

[89] L.J. Tacconi, R. Genzel, A. Saintonge, F. Combes, S. García-Burillo, R. Neri et al., *PHIBSS: Unified Scaling Relations of Gas Depletion Time and Molecular Gas Fractions*, *ApJ* **853** (2018) 179 [[1702.01140](#)].

[90] S. Wuyts, N.M. Förster Schreiber, A. van der Wel, B. Magnelli, Y. Guo, R. Genzel et al., *Galaxy Structure and Mode of Star Formation in the SFR-Mass Plane from $z \sim 2.5$ to $z \sim 0.1$* , *ApJ* **742** (2011) 96 [[1107.0317](#)].

[91] S. Gurovich, K. Freeman, H. Jerjen, L. Staveley-Smith and I. Puerari, *The Slope of the Baryonic Tully-Fisher Relation*, *AJ* **140** (2010) 663 [[1004.4365](#)].

[92] K. Freeman, *On the disks of spiral and s0 galaxies*, *The Astrophysical Journal* **160** (1970) 811.

[93] J. Fu, Q. Guo, G. Kauffmann and M.R. Krumholz, *The atomic-to-molecular transition and its relation to the scaling properties of galaxy discs in the local Universe*, *Monthly Notices of the Royal Astronomical Society* **409** (2010) 515 [<https://academic.oup.com/mnras/article-pdf/409/2/515/18577070/mnras0409-0515.pdf>].

[94] A.K. Leroy, F. Walter, E. Brinks, F. Bigiel, W.J.G. de Blok, B. Madore et al., *The Star Formation Efficiency in Nearby Galaxies: Measuring Where Gas Forms Stars Effectively*, *AJ* **136** (2008) 2782 [[0810.2556](#)].

[95] D. Cormier, F. Bigiel, J. Wang, J. Pety, A. Usero, S. Roychowdhury et al., *The Bluedisk survey: molecular gas distribution and scaling relations in the context of galaxy evolution*, *Monthly Notices of the Royal Astronomical Society* **463** (2016) 1724 [<https://academic.oup.com/mnras/article-pdf/463/2/1724/9685978/stw2097.pdf>].

[96] P. Dimauro, M. Huertas-Company, E. Daddi, P.G. Pérez-González, M. Bernardi, G. Barro et al., *A catalog of polychromatic bulge-disc decompositions of $\sim 17,600$ galaxies in CANDELS*, *MNRAS* **478** (2018) 5410 [[1803.10234](#)].

[97] L. Morselli, P. Popesso, G. Erfanianfar and A. Concas, *Bulges and discs in the local Universe. Linking the galaxy structure to star formation activity*, *A&A* **597** (2017) A97 [[1607.07675](#)].

[98] J.T. Mendel, L. Simard, M. Palmer, S.L. Ellison and D.R. Patton, *A Catalog of Bulge, Disk, and Total Stellar Mass Estimates for the Sloan Digital Sky Survey*, *ApJS* **210** (2014) 3 [[1310.8304](#)].

[99] L. Hernquist, *An Analytical Model for Spherical Galaxies and Bulges*, *ApJ* **356** (1990) 359.

[100] D.S.H. Hon, A.W. Graham and N. Sahu, *The size-mass and other structural parameter (n , μ_z , R_z) relations for local bulges/spheroids from multicomponent decompositions*, *MNRAS* **519** (2023) 4651 [[2209.01550](#)].

[101] P. Dimauro, M. Huertas-Company, E. Daddi, P.G. Pérez-González, M. Bernardi, F. Caro et al., *The structural properties of classical bulges and discs from $z \sim 2$* , *MNRAS* **489** (2019) 4135 [[1902.04089](#)].

[102] J. Leja, B.D. Johnson, C. Conroy, P. van Dokkum, J.S. Speagle, G. Brammer et al., *An Older, More Quiescent Universe from Panchromatic SED Fitting of the 3D-HST Survey*, *ApJ* **877** (2019) 140 [[1812.05608](#)].

[103] C. Pacifici, K.G. Iyer, B. Mobasher, E. da Cunha, V. Acquaviva, D. Burgarella et al., *The Art of Measuring Physical Parameters in Galaxies: A Critical Assessment of Spectral Energy Distribution Fitting Techniques*, *ApJ* **944** (2023) 141 [[2212.01915](#)].

[104] Y.-Y. Chang, A. van der Wel, E. da Cunha and H.-W. Rix, *Stellar Masses and Star Formation Rates for 1M Galaxies from SDSS+WISE*, *ApJS* **219** (2015) 8 [[1506.00648](#)].

[105] E.J. Nelson, S. Tacchella, B. Diemer, J. Leja, L. Hernquist, K.E. Whitaker et al., *Spatially resolved star formation and inside-out quenching in the TNG50 simulation and 3D-HST observations*, *MNRAS* **508** (2021) 219 [[2101.12212](#)].

[106] A. Chowdhury, N. Kanekar and J.N. Chengalur, *Atomic Gas Scaling Relations of Star-forming Galaxies at $z \approx 1$* , *ApJL* **941** (2022) L6 [[2212.06176](#)].

[107] F. Acero, J.T. Acquaviva, R. Adam, N. Aghanim, M. Allen, M. Alves et al., *French SKA White Book - The French Community towards the Square Kilometre Array*, *arXiv e-prints* (2017) arXiv:1712.06950 [[1712.06950](#)].

[108] M.G. Labate, M. Waterson, B. Alachkar, A. Hendre, P. Lewis, M. Bartolini et al., *Highlights of the Square Kilometre Array Low Frequency (SKA-LOW) Telescope*, *Journal of Astronomical Telescopes, Instruments, and Systems* **8** (2022) 011024.

[109] K.A. Oman, A. Marasco, J.F. Navarro, C.S. Frenk, J. Schaye and A. Benítez-Llambay, *Non-circular motions and the diversity of dwarf galaxy rotation curves*, *MNRAS* **482** (2019) 821 [[1706.07478](#)].

[110] M. Petač, *Equilibrium axisymmetric halo model for the Milky Way and its implications for direct and indirect dark matter searches*, *PRD* **102** (2020) 123028 [[2008.11172](#)].

[111] A. Tamm, E. Tempel, P. Tenjes, O. Tikhonova and T. Tuvikene, *Stellar mass map and dark matter distribution in M 31*, *A&A* **546** (2012) A4 [[1208.5712](#)].

[112] P.G. van Dokkum and M. Franx, *Morphological Evolution and the Ages of Early-Type Galaxies in Clusters*, *arXiv e-prints* (2001) astro [[astro-ph/0101468](#)].

[113] S.J. Lilly and C.M. Carollo, *Surface Density Effects in Quenching: Cause or Effect?*, *ApJ* **833** (2016) 1 [[1604.06459](#)].

[114] W.J.C. de Blok and S.S. McGough, *Dark Matter in Low Surface Brightness Galaxies*, in *Dark and Visible Matter in Galaxies and Cosmological Implications*, M. Persic and P. Salucci, eds., vol. 117 of *Astronomical Society of the Pacific Conference Series*, p. 39, Jan., 1997, DOI [[astro-ph/9610216](#)].

[115] A.A. Dutton, F.C. van den Bosch, A. Dekel and S. Courteau, *A Revised Model for the Formation of Disk Galaxies: Low Spin and Dark Halo Expansion*, *ApJ* **654** (2007) 27 [[astro-ph/0604553](#)].

[116] F. Lelli, S.S. McGaugh and J.M. Schombert, *SPARC: Mass Models for 175 Disk Galaxies with Spitzer Photometry and Accurate Rotation Curves*, *AJ* **152** (2016) 157 [[1606.09251](#)].

[117] I. Breda and P. Papaderos, *The continuous rise of bulges out of galactic disks*, *A&A* **614** (2018) A48 [[1712.05354](#)].

[118] M. Vogelsberger, F. Marinacci, P. Torrey and E. Puchwein, *Cosmological simulations of galaxy formation*, *Nature Reviews Physics* **2** (2020) 42 [[1909.07976](#)].

[119] P.G. van Dokkum, J. Leja, E.J. Nelson, S. Patel, R.E. Skelton, I. Momcheva et al., *The Assembly of Milky-Way-like Galaxies Since $z \sim 2.5$* , *ApJL* **771** (2013) L35 [[1304.2391](#)].

[120] R.C. Tolman, *On the Estimation of Distances in a Curved Universe with a Non-Static Line Element*, *Proceedings of the National Academy of Science* **16** (1930) 511.

[121] M.A. Pahre, S.G. Djorgovski and R.R. de Carvalho, *A Tolman Surface Brightness Test for Universal Expansion and the Evolution of Elliptical Galaxies in Distant Clusters*, *ApJL* **456** (1996) L79 [[astro-ph/9511061](#)].

[122] A. Sandage, *The Tolman Surface Brightness Test for the Reality of the Expansion. V. Provenance of the Test and a New Representation of the Data for Three Remote Hubble Space Telescope Galaxy Clusters*, *AJ* **139** (2010) 728 [[0905.3199](#)].

[123] A. Puglisi, U. Dudzevičiūtė, M. Swinbank, S. Gillman, A.L. Tiley, R.G. Bower et al., *KURVS: the outer rotation curve shapes and dark matter fractions of $z \approx 1.5$ star-forming galaxies*, *MNRAS* **524** (2023) 2814 [[2305.04382](#)].

[124] M.R. Lovell, A. Pillepich, S. Genel, D. Nelson, V. Springel, R. Pakmor et al., *The fraction of dark matter within galaxies from the IllustrisTNG simulations*, *MNRAS* **481** (2018) 1950 [[1801.10170](#)].

[125] R.H. Wechsler and J.L. Tinker, *The Connection Between Galaxies and Their Dark Matter Halos*, *ARAA* **56** (2018) 435 [[1804.03097](#)].

[126] R.J. Wright, C.d.P. Lagos, C. Power and P.D. Mitchell, *The impact of stellar and AGN feedback on halo-scale baryonic and dark matter accretion in the EAGLE simulations*, *MNRAS* **498** (2020) 1668 [[2006.00924](#)].

[127] A.-M. Weijmans, D. Krajnović, G. Van De Ven, T.A. Oosterloo, R. Morganti and P. De Zeeuw, *The shape of the dark matter halo in the early-type galaxy NGC 2974*, *Monthly Notices of the Royal Astronomical Society* **383** (2008) 1343.

[128] K.G. Noeske, B.J. Weiner, S.M. Faber, C. Papovich, D.C. Koo, R.S. Somerville et al., *Star Formation in AEGIS Field Galaxies since $z=1.1$: The Dominance of Gradually Declining Star Formation, and the Main Sequence of Star-forming Galaxies*, *ApJL* **660** (2007) L43 [[astro-ph/0701924](#)].

[129] K.E. Whitaker, P.G. van Dokkum, G. Brammer and M. Franx, *The Star Formation Mass Sequence Out to $z = 2.5$* , *ApJL* **754** (2012) L29 [[1205.0547](#)].

[130] G. Rodighiero, E. Daddi, I. Baronchelli, A. Cimatti, A. Renzini, H. Aussel et al., *The Lesser Role of Starbursts in Star Formation at $z = 2$* , *ApJL* **739** (2011) L40 [[1108.0933](#)].

[131] N.M. Förster Schreiber, R. Genzel, M.D. Lehnert, N. Bouché, A. Verma, D.K. Erb et al., *SINFONI Integral Field Spectroscopy of $z \sim 2$ UV-selected Galaxies: Rotation Curves and Dynamical Evolution*, *ApJ* **645** (2006) 1062 [[astro-ph/0603559](#)].

[132] E. Daddi, D. Elbaz, F. Walter, F. Bournaud, F. Salmi, C. Carilli et al., *Different Star Formation Laws for Disks Versus Starbursts at Low and High Redshifts*, *ApJL* **714** (2010) L118 [[1003.3889](#)].

[133] R. Genzel, L.J. Tacconi, D. Lutz, A. Saintonge, S. Berta, B. Magnelli et al., *Combined CO and Dust Scaling Relations of Depletion Time and Molecular Gas Fractions with Cosmic Time, Specific Star-formation Rate, and Stellar Mass*, *ApJ* **800** (2015) 20 [[1409.1171](#)].

[134] J. Freundlich, F. Combes, L.J. Tacconi, R. Genzel, S. García-Burillo, R. Neri et al., *PHIBSS2: survey design and $z = 0.5 - 0.8$ results. Molecular gas reservoirs during the winding-down of star formation*, *A&A* **622** (2019) A105 [[1812.08180](#)].

[135] A. Bianchetti, F. Sinigaglia, G. Rodighiero, E. Elson, M. Vaccari, D.J. Pisano et al., *New Constraints on the Evolution of the $M_{HI}-M_{\star}$ Scaling Relation Combining CHILES and MIGHTEE-H I Data*, *ApJ* **982** (2025) 82 [[2502.00110](#)].

[136] M. Cappellari, *Full spectrum fitting with photometry in PPXF: stellar population versus dynamical masses, non-parametric star formation history and metallicity for 3200 LEGA-C galaxies at redshift $z \approx 0.8$* , *MNRAS* **526** (2023) 3273 [[2208.14974](#)].

[137] A. Vazdekis, P. Sánchez-Blázquez, J. Falcón-Barroso, A.J. Cenarro, M.A. Beasley, N. Cardiel et al., *Evolutionary stellar population synthesis with MILES - I. The base models and a new line index system*, *MNRAS* **404** (2010) 1639 [[1004.4439](#)].